Monthly Notices of the ROYAL ASTRONOMICAL SOCIETY

MNRAS **547,** 1–27 (2026) https://doi.org/10.1093/mnras/staf1517
Advance Access publication 2025 September 10

SN 2023xgo: Helium-rich Type Icn or Carbon-Flash Type Ibn supernova?

Anjasha Gangopadhyay [1★] Jesper Sollerman [1] Konstantinos Tsalapatas [1] Keiichi Maeda [2] Naveen Dukiya [3,4] Steve Schulze [5] Claes Fransson [1] Nikhil Sarin [6] Priscila J. Pessi [1] Mridweeka Singh [7] Jacob Wise [8] Tatsuya Nakaoka,[9] Avinash Singh [1] Raya Dastidar [10,11] Miho Kawabata [2] Yu-Jing Qin,[12] Kaustav K. Das [12] Daniel Perley [8] Christoffer Fremling [13] Kenta Taguchi [2] K-Ryan Hinds [8] Ragnhild Lunnan [1] Rishabh Singh Teja [7] Monalisa Dubey [3] Bhavya Ailawadhi [3] Smaranika Banerjee [1] Koji S. Kawabata [9] Kuntal Misra [3] Devendra K. Sahu [7] Sea'n J. Brennan [1] Mansi M. Kasliwal [14] Anna Y. C. Q Ho [15] Aleksandra Bochenek [8] Ben Rusholme [16] Russ R. Laher [16] Roger Smith [13] Josiah Purdum[13] and Niharika Sravan[17]

Affiliations are listed at the end of the paper

Accepted 2025 September 6. Received 2025 August 15; in original form 2025 June 12

ABSTRACT

We present observations of SN 2023xgo, a transitional Type Ibn/Icn SN, from −5.6 to 63 d relative to r-band peak. Early spectra show C III λ5696 emission like Type Icn SNe, shifting to Type Ibn features. The He I velocities (1800–10 000 km s^{-1}) and pseudo-equivalent widths are among the highest in the Ibn/Icn class. The light curve declines at 0.14 mag d^{-1} until 30 d, matching SNe Ibn/Icn but slower than fast transients. SN 2023xgo is the faintest in our SN Ibn sample ($M_r = -17.65 \pm 0.04$) but shows typical colour and host properties. Semi-analytical modelling of the light curve suggests a compact CSM shell ($\sim 10^{12}$–10^{13} cm), mass-loss rate between 10^{-4} and 10^{-3} M$_\odot$ yr^{-1} with CSM and ejecta masses of ∼0.22 and 0.12 M$_\odot$, respectively. Post-maximum light-curve, spectral modelling favours a ∼3 M$_\odot$ helium star progenitor with extended ($\sim 10^{15}$ cm), stratified CSM (density exponent of 2.9) and mass-loss rate of $0.1 - 2.7$ M$_\odot$ yr^{-1}. These two mass-loss regimes imply a radially varying CSM, shaped by asymmetry or changes in the progenitor's mass-loss over time. This mass-loss behaviour fits both binary and single-star evolution. Early Icn-like features stem from hot carbon ionization, fading to Ibn-like with cooling. SN 2023xgo thus offers rare insight into the connection between SNe Icn, Ibn, and SNe Ibn with ejecta signatures.

Key words: techniques: imaging spectroscopy – supernovae: general – galaxies: photometry.

1 INTRODUCTION

Interacting stripped-envelope (SE) supernovae (SNe) is a relatively new family of SNe (see for example N. Smith (see for example N. Smith 2017; M. Fraser 2020; A. Gangopadhyay 2024; L. Dessart 2024). Whereas Type Ib SNe are classified by their spectral lack of hydrogen – and presence of helium – their interacting counterparts, SNe Ibn, display clear narrow helium lines, but no or weak lines of narrow hydrogen. Type Icn SNe (A. Gal-Yam et al. 2022; D. A. Perley et al. 2022) are even rarer explosions characterized by narrow carbon and nitrogen lines, but lack hydrogen and helium lines.

The progenitors of Type Ib/c SNe must somehow have lost their outer hydrogen envelope before explosion, and the Type Ibn SNe clearly interact with helium-rich circumstellar material (CSM) previously lost by their progenitor stars. The rare subclasses of interacting SESNe thus hold great potential to explore progenitor systems and mass-loss mechanisms of massive stars (S. E. Woosley & T. A. Weaver 1995). However, this picture faces challenges. First of all, the ejected masses deduced from comparison of SN Ib/c light curves with hydrodynamical models are only a few solar masses, which are much lower than predicted for exploding single Wolf–Rayet (WR) stars. No massive WR star has been seen in direct imaging in pre-explosion sites (C. D. Kilpatrick & R. J. Foley 2018; S. D. Van Dyk et al. 2018) of SESNe except iPTF13bvn (Y. Cao et al. 2013; C. Fremling et al. 2014), and SNe Ib/c are too abundant by a factor of ∼2 to originate from the WR population alone (N. Smith et al. 2011). For these reasons, binary evolution could be a likely progenitor scenario for SESNe. For SNe Ibn, the velocities inferred from the width of the narrow helium lines attributed to the dense CSM surrounding the progenitor stars are comparable with velocities seen in the winds of local group of WR stars. However, the inferred mass-loss rates in SNe Ibn are much higher than those seen in WR stars, and indicate that the progenitors might have undergone an enhanced phase of episodic mass-loss (A. Pastorello et al. 2007).

Type Ibn/Icn SNe often display rapid light-curve evolution, with a fast rise and often also a rapid decline (G. Hosseinzadeh et al. 2017; A. Gal-Yam et al. 2022), and can be quite luminous (−16

★ E-mail: anjasha.gangopadhyay@astro.su.se

to −20 mag). It has therefore been argued that the underlying powering mechanism cannot be only due to radioactive nickel as in the non-interacting SESNe but that the CSM interaction visible in the spectral evolution contributes to the overall luminosity. The fast, blue, luminous nature of the light curves of these SNe show resemblance with Fast Blue Optical Transients (FBOTs) or Rapidly Evolving Transients (RETs) (M. R. Drout et al. 2014; A. Y. Q. Ho et al. 2023). However, there are also some slow evolving Type Ibn SN candidates like OGLE-12-SN-006 (A. Pastorello et al. 2015b), which shows a rise time of about 2 weeks.

The diversity in the population and the relatively low numbers of known objects mean that the boundaries between the subclassifications are still somewhat fuzzy. Spectroscopically, even if SNe Ibn show narrow emission lines of helium, some SNe Ibn have residual hydrogen in their spectra (e.g. ASASSN-15ed; A. Pastorello et al. 2015c, SN 2019wep; A. Gangopadhyay et al. 2022). A. Gangopadhyay et al. (2025) discuss the continuity between SNe IIn (with narrow hydrogen lines) and SNe Ibn (narrow He lines around maximum light). M. Pursiainen et al. (2023) presented the case of SN 2023emq, which was initially classified as a SN Icn but shows prominent He I lines later on. S. Schulze et al. (2025) suggest a new fully stripped class, SNe Ien, with narrow silicon, sulphur, and argon lines. These classes may not be distinct, but could be somehow linked by the continuity in the properties of the outer envelopes of their progenitors. A detailed investigation of these SNe would be valuable for probing how mass-loss occurs during the final stages and for providing insights into the chemical structure of the progenitors.

Some SNe Ibn may show additional emission lines early on, similar to the flash spectroscopy lines sometimes seen in early Type II SN spectra (A. Gal-Yam et al. 2014). Some examples of these are SNe 2010al (A. Pastorello et al. 2015a), 2019uo (A. Gangopadhyay et al. 2020), and 2019cj (Z. Y. Wang et al. 2024). Also for SN 2023emq, M. Pursiainen et al. (2023) portrays the event as a flash ionized SN Ibn because it shows the C III λ5696 feature only early on. SNe Icn also show helium signatures, but very feeble and late in its evolution (D. A. Perley et al. 2022). In this paper, we present the analysis of SN 2023xgo, a nearby but relatively faint member of the SN Ibn/Icn family. We discuss whether it should be regarded as a member of the Type Icn class, although it may have some residual helium, or if it is better characterized as a flash ionized Type Ibn SN with long-lived carbon emission.

The paper is organized as follows. In Section 2, we present our comprehensive set of optical photometry and spectroscopy together with the data reduction procedures. Section 3 presents the spectroscopic analysis of SN 2023xgo, matching and comparing with a group of SNe Ibn and SNe Icn. Section 4 presents the host Galaxy analysis of the SN. Section 5 presents the light-curve evolution and comparison with another group of SNe Ibn/Icn from the literature. In particular, we investigate if CSM interaction is required to power the light curve (Section 6) by fitting analytical/semi-analytical models at early and late phases. We discuss our results and the general scenario for SN 2023xgo in Section 7 and summarize our conclusions in Section 8.

1.1 Discovery and classification

SN 2023xgo was discovered by the Zwicky Transient Facility (ZTF) as ZTF23abprwou on 2023 November 9 and immediately reported to the Transient Name Server by C. Fremling (2023). The report mentions that the object at RA 05:04:19.183, DEC + 67:37:21.04 (J2000.0) was first detected in the ZTF *r*-band at a magnitude of 18.56 on 2023 November 9 06:44:38.40 UT, while the last non-detection

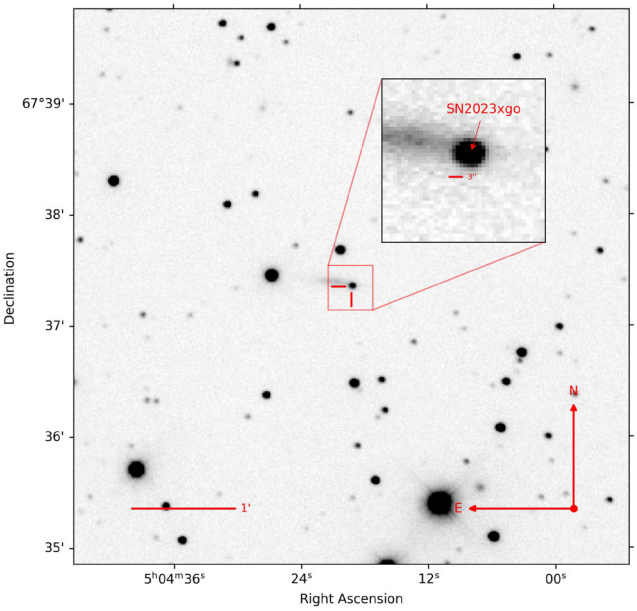

Figure 1. An image of SN 2023xgo taken with the 1.3 m Devasthal Fast Optical Telescope, ARIES, India in the *R* band on 2023 November 21. The SN is 2.6 kpc away from the centre of the host Galaxy and is well detected in the image (highlighted in the inset).

($g > 20.41$) was from three days earlier, on 2023 November 6. SN 2023xgo was initially classified as a Type Icn SN (C. Balcon 2023) based on a low-resolution spectrum from a 0.41 m telescope obtained on 2023 November 11, in the course of the Italian Supernovae Search Project. The spectrum was reported to show a blue continuum with probable C III emission at a redshift of $z = 0.014$, resembling SN 2023emq (M. Pursiainen et al. 2023). We later re-classified the SN on TNS as a Type Ibn SN based on the P200 spectrum (Section 3) obtained on 2023 December 3 (J. Sollerman et al. 2023). An image showing the precise location of the SN in its host Galaxy is shown in Fig. 1.

1.2 Explosion epoch

To estimate the explosion epoch, we fitted a parabolic function to the rising part of the *g*-band light curve. The early light-curve shape is well reproduced by a parabola. We performed the fit using 50 000 iterations of Markov Chain Monte-Carlo (MCMC) simulations. Using this method, we find the explosion epoch to be MJD 60257.22 ± 0.5, which is 0.5 d prior to the first detection. This estimate is also consistent with the last non-detection of the source. We thus adopt that the explosion occurred 0.5 d before the first detection of the SN.

1.3 Extinction and distance

The Milky Way extinction along the line of sight to SN 2023xgo is $A_V = 0.456$ mag (from NASA Extragalactic Database[1]). We adopted this Milky Way reddening from E. F. Schlafly & D. P. Finkbeiner (2011), applied an extinction law from J. A. Cardelli, G. C. Clayton & J. S. Mathis (1989) assuming an R_V of 3.1. The Na ID lines are very faint throughout the spectral evolution of SN 2023xgo. To estimate the extinction from the host Galaxy, we estimated the equivalent

[1] https://ned.ipac.caltech.edu

width of the Na ID lines in the moderate resolution DBSP spectrum taken on 2023 November 15 (R ∼1200–1500), where we could detect a line at a signal-to-noise ratio of 13 (Section 2.4). Using the formulation by D. Poznanski, J. X. Prochaska & J. S. Bloom (2012), we estimate the extinction of the host Galaxy as $A_V = 0.043 \pm 0.011$ mag assuming R_V of 3.1. The value quoted for A_V from the host is then multiplied by 0.86 to make it consistent with the recalibration of the Milky Way extinction by E. F. Schlafly & D. P. Finkbeiner (2011). Thus, we adopt a total $A_V = 0.49 \pm 0.01$ mag along the line of sight, considering both the contribution from the Milky Way and from the host Galaxy.

There is no previously known redshift for the host Galaxy. We measure the redshift of SN 2023xgo fro

m the narrow emission lines of the host Galaxy, which gives $z = 0.01325$ (Section 2.4). Adopting $H_0 = 73\,\mathrm{km\,s^{-1}\,Mpc^{-1}}$ (A. G. Riess et al. 2011), $\Omega_m = 0.27$ and $\Omega_{vac} = 0.73$, we obtain the distance to be 54.4 ± 1.4 Mpc, and a distance modulus of 33.68 ± 0.06 mag. J. Carrick et al. (2015) found a peculiar velocity on the order of 100 km s^{-1}. The peculiar velocity associated could contribute to the distance uncertainty, and we consider this as part of the error in both the distance and distance modulus. We use this value throughout the article.

2 OBSERVATIONS AND DATA REDUCTIONS

2.1 Optical and infrared photometry

We observed SN 2023xgo in the *uvBVRIgrizJHK* bands from day −5.6 to ∼63 d post r-band maximum (in the observer frame of reference) (see Section 5). The photometry of SN 2023xgo in the gri-bands was obtained using the ZTF camera (R. Dekany et al. 2020) on the Palomar 48 inch (P48) telescope and also with the Palomar 60 inch Rainbow Camera. The Zwicky Transient Facility (E. C. Bellm et al. 2019; M. J. Graham et al. 2019) surveys the entire observable northern sky with a typical 2-d cadence in g- and r-band. The rise of the SN light curve was covered in the ZTF data, and complemented this with r-band data from the P60 Rainbow Camera. The P60 data were reduced with the `FPipe` pipeline described in C. Fremling et al. (2016). The ZTF forced point spread function (PSF)-fit photometry was requested from the Infrared Processing and Analysis Center (F. J. Masci et al. 2019) for the P48 gri-bands. To obtain the light curve, we follow the ZTF data processing procedure[2] including baseline correction, validation of flux uncertainties, combining measurements obtained on the same night, and converting the differential fluxes to the AB magnitude system.

Optical photometric observations of SN 2023xgo in $griz$-bands were also performed using the robotic 0.7 m GROWTH-India telescope (GIT; H. Kumar et al. 2022) located at the Indian Astronomical Observatory (IAO) in Hanle, India. The observations were carried out in the Sloan Digital Sky Survey (SDSS) $griz$-bands beginning 2023 May 20. The data were processed with the standard GIT image processing pipeline described in H. Kumar et al. (2022), and the steps followed are described in R. S. Teja et al. (2023).

SN 2023xgo was observed using the 1.3 m Devasthal Fast Optical Telescope (DFOT) in $BVRI$-filters. The bias and flat-field corrections were done following the standard procedures using `ccdproc` (M. Craig et al. 2017), and cosmic ray removal was done using `astrosrappy` (P. G. Dokkum 2001; C. McCully & M. Tewes 2019). Image subtraction was performed using High Order Transform of PSF ANd Template Subtraction (HOTPANTS; A. Becker 2015) with the reference images taken after the SN had faded. The PSF photometry on the subtracted image was performed using a custom `PSFEx` (E. Bertin 2013) and `photutils` (L. Bradley et al. 2024) based pipeline. A local star sequence was calibrated using Landolt fields observed on the same night, which was used to calibrate the *BVRI* instrumental magnitudes to apparent magnitudes.

The SN was also monitored with the 2.0 m Liverpool Telescope (LT; I. A. Steele et al. 2004) using the IO:O imager at the Roque de los Muchachos Observatory in the $griz$-bands. The images were retrieved from the LT data archive[3] and processed through a PSF photometry script developed by Hinds and Taggart et al. (in preparation), and subtracting the host Galaxy contribution from the images. Each measurement was calibrated using stars from the Pan-STARRS (H. A. Flewelling et al. 2020) catalogue.

One epoch of photometry in the gr-bands was obtained with the Alhambra Faint Object Spectrograph and Camera (ALFOSC) at the 2.56 m Nordic Optical Telescope (NOT). For the reduction, the `PyNOT`[4] data processing pipeline was utilized. In case of multiple exposures, we computed the weighted average of the magnitudes estimated from different images with the same filter setup.

Imaging observations in $BVRIJHK$-bands were also carried out using the 1.5 m Kanata telescope (KT; K. S. Kawabata et al. 2008) of Hiroshima University in Japan. We used the standard tasks available in the data reduction software `IRAF` (D. Tody 1986) for carrying out the pre-processing. Multiple frames were taken on some nights and co-added in respective bands after the geometric alignment of the images to increase the signal-to-noise ratio, and then template subtracted photometry was performed to obtain the magnitudes. A smaller version of the photometry table in reported in Table A1.

2.2 Ultraviolet photometry from *Swift*

The Ultraviolet Optical Telescope (UVOT; P. W. A. Roming et al. 2005) onboard the Neil Gehrels *Swift* Observatory (N. Gehrels et al. 2004) monitored SN 2023xgo in four epochs. We analysed these data with the online tools of the UK *Swift* team[5] that use the software package `HEASoft`[6] version 6.26.1 and methods described in P. A. Evans et al. (2007, 2009). Since the host Galaxy was faint for SN 2023xgo, we did not use the host subtracted photometry and used the full, unsubtracted light curve for our analysis.

2.3 X-ray observations from *Swift*

While monitoring SN 2023xgo with UVOT, *Swift* also observed the field with its onboard X-ray telescope XRT between 0.3 and 10 keV in photon-counting mode (D. N. Burrows et al. 2005). The X-ray data was reduced using the same technique as the UV data. SN 2023xgo evaded detection at all epochs. The median 3σ count-rate limit of each observing block is 9×10^{-3} s^{-1} (0.3–10 keV). Coadding all data pushes the 3σ count-rate limits to 1.2×10^{-3} s^{-1}. To convert the count-rate limits into a flux, we assume a power-law spectrum with a photon index[7] of $\Gamma = 2$ and a Galactic neutral

[2] https://irsa.ipac.caltech.edu/data/ZTF/docs/ZTF_zfps_userguide.pdf

[3] https://telescope.livjm.ac.uk/cgi-bin/lt_search

[4] https://github.com/jkrogager/PyNOT

[5] https://www.swift.ac.uk/user_objects

[6] https://heasarc.gsfc.nasa.gov/docs/software/heasoft/

[7] The photon index is defined as the power-law index of the photon flux density ($N(E) \propto E^{-\Gamma}$).

hydrogen column density of 9.1×10^{20} cm^{-2} (HI4PI Collaboration et al. 2016). The coadded count-rate limit translates to an unabsorbed flux of $< 0.54 \times 10^{-13}$ erg cm^{-2} s^{-1} in the range of $0.3 - 10$ keV and a luminosity of $< 2 \times 10^{40}$ erg s^{-1}.

2.4 Spectroscopic observations

In the course of our follow-up campaign of SN 2023xgo we obtained 20 spectra ranging from −2.35 to 23.48 d post r-band maximum (in the observer frame of reference). We obtained eight epochs of spectroscopy with the Spectral Energy Distribution Machine (SEDM; N. Blagorodnova et al. 2018) mounted on the Palomar 60-inch telescope. The SEDM data were reduced using the pipeline described in M. Rigault et al. (2019); Y. L. Kim et al. (2022). We used the Double Beam Spectrograph (DBSP; J. B. Oke & J. E. Gunn 1982; M. S. Mandigo-Stoba, C. Fremling & M. M. Kasliwal 2021, 2022a, b) on the Palomar 200-inch telescope to obtain two spectra of SN 2023xgo. The data reduction was done using a custom DBSP data reduction pipeline (A. S. Piascik et al. 2014; M. Roberson, C. Fremling & M. Kasliwal 2022) relying on `Pypeit` (J. X. Prochaska et al. 2019; J. X. Prochaska et al. 2020, 2021). We obtained two epochs of spectroscopy with the Low-Resolution Imaging Spectrometer (LRIS; J. B. Oke et al. 1995) on the Keck I telescope, with data reduced using `lpipe` (D. A. Perley et al. 2019). We also got a single spectrum with the Spectrograph for the Rapid Acquisition of Transients (SPRAT; A. S. Piascik et al. 2014) on the 2.0 m Liverpool Telescope (LT). This spectrum was reduced and flux calibrated using a custom `Python` pipeline for the LT, utilizing the packages `Astropy` (Astropy Collaboration 2022), `Matplotlib` (J. D. Hunter 2007), `NumPy` (S. Walt, S. C. Colbert & G. Varoquaux 2011), and `SciPy` (P. Virtanen et al. 2020). Cosmic rays were corrected using the L.A.Cosmic algorithm (P. G. Dokkum 2001). The standard star Feige 34 (J. B. Oke 1990), observed on the same night, was used for flux calibration, with differences in the airmass of the standard star and science frames corrected by applying table 1 from La Palma Technical Note No. 31.[8] Observations using these telescopes/instruments were coordinated using the `FRITZ` data platform (S. J. Walt, A. Crellin-Quick & J. S. Bloom 2019; M. W. Coughlin et al. 2023).

Additionally, spectroscopic observations were carried out using the Himalayan Faint Object Spectrograph and Camera (HFOSC) mounted on the Himalayan Chandra Telescope (HCT; T. P. Prabhu & G. C. Anupama 2010) and KOOLS-IFU (K. Matsubayashi et al. 2019) on the Seimei Telescope. For HCT, we used a 2 arcsec wide slit and Grisms Gr7/Gr8 for taking optical spectra. The spectra taken with HFOSC were reduced using the *twodspec* package in `IRAF`, followed by wavelength and flux calibration. The spectra with KOOLS-IFU were taken through optical fibers and the VPH-blue grism. The data reduction was performed using the `Hydra` package in `IRAF` (S. C. Barden 1994) and a reduction software developed for KOOLS-IFU data.[9]

The slit loss corrections for all the spectra were done by scaling the spectra with respect to the SN photometry. The collage of all the spectra is shown in Fig. 2, and the spectroscopy log can be found in Table A2.

[8] https://www.ing.iac.es/Astronomy/observing/manuals/ps/tech_notes/tn031.pdf
[9] http://www.o.kwasan.kyoto-u.ac.jp/inst/p-kools

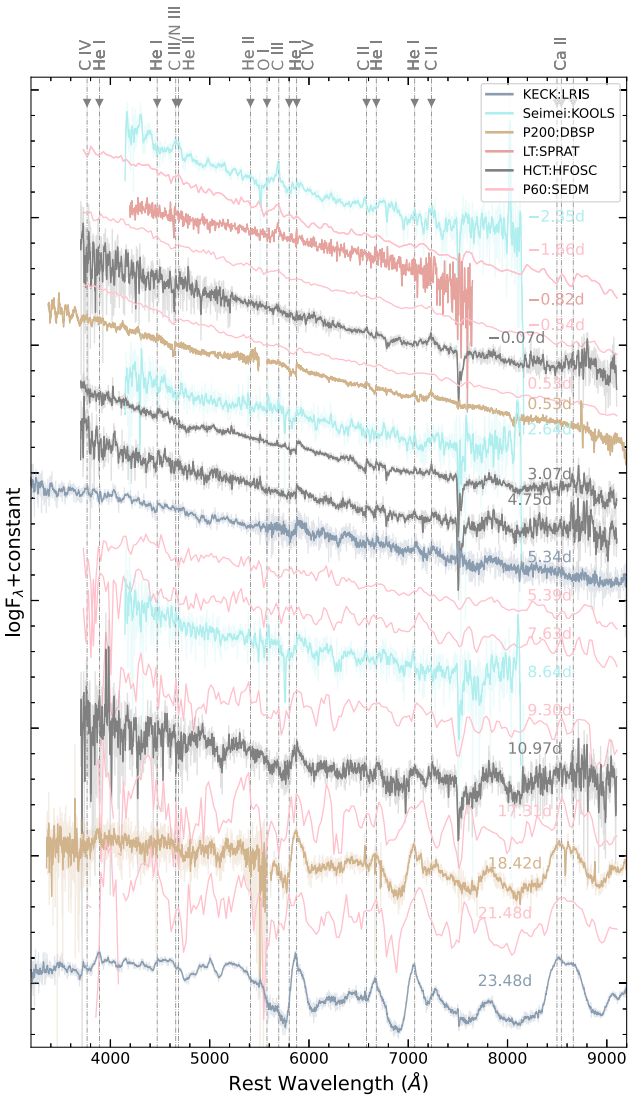

Figure 2. The complete spectral evolution of SN 2023xgo from −2.35 to 23.48 d post maximum. The phase is calculated with respect to the r-band maximum (MJD = 60262.86 ± 0.46). The colours represent different telescopes and instruments (Table A2). The dark coloured spectrum is the smoothed version of the original spectrum shown in light-shaded colours.

3 SPECTROSCOPIC EVOLUTION

The complete spectral evolution of SN 2023xgo from −2.35 to 23.48 d post r-band maximum is shown in Fig. 2. The early spectral sequence of SN 2023xgo shows a blue continuum. The earliest spectrum of SN 2023xgo at −2.35 d shows a number of flash ionization lines from the recombination of the CSM. Three peaks are seen at 4655, 4685, and 5680 Å in the earliest spectrum of SN 2023xgo. The bluest peak arises due to a blend of C III/N III, and the peak at 4685 Å is due to He II λ4686. The C III/N III and He II lines are common flash ionized lines for SNe Icn (A. Gal-Yam et al. 2022; C. Pellegrino et al. 2022b) and SNe Ibn (A. Gangopadhyay et al. 2020, 2022). However, although the third peak at 5696 Å of C III is common for SNe Icn, its strength is less for the SN Icn 2023emq (M. Pursiainen et al. 2023), which transitioned to SN Ibn. The feature is rarely seen in SNe Ibn with prominence. SN 2023xgo exhibits one

of the strongest C III λ5696 lines for the SN Ibn subtype. The flash ionization lines are seen until 2.64 d in the spectral evolution.

The overall spectral evolution of SN 2023xgo indicates that it could be a transitional SN Ibn/Icn. The SN behaved like a SN Icn early on with strong carbon features and then transformed to a SN Ibn around maximum light with carbon disappearing and narrow helium lines appearing. It is not known whether most SNe Ibn show early spectroscopic signatures like this, or to what time-scales SNe Ibn can show flash ionization signatures.

3.1 Pre-maximum spectral evolution

We proceeded to compare the earliest spectrum of SN 2023xgo with a sample of SNe IIn, Ibn, and Icn, which showed signatures of flash ionization (A. Gal-Yam et al. 2014) in their early spectra. Among the SNe Ibn, we selected SNe 2010al (A. Pastorello et al. 2015a), 2018bcc (E. Karamehmetoglu et al. 2021), 2019uo (A. Gangopadhyay et al. 2020), and 2019wep (A. Gangopadhyay et al. 2022). Among the SNe Icn, we compared the earliest spectrum of SN 2023xgo with SNe 2021ckj (T. Nagao et al. 2023) and 2021csp (D. A. Perley et al. 2022). We also compared SN 2023xgo with the flash ionized Type IIn SN 1998S (A. Fassia et al. 2001) and with SN 2023emq (M. Pursiainen et al. 2023), where the latter is also a candidate to show transitional signatures between SN Ibn and SN Icn sub-classes.

The early spectral comparison of SN 2023xgo is shown in Fig. 3. All the comparison spectra were downloaded from Wiserep (O. Yaron & A. Gal-Yam 2012) and corrected for the redshift of the host Galaxy. All the SNe IIn, Ibn and SN 2023emq in this sample show an emission feature around 4650 Å due to a blend of C III, N III and He II, similar to what we observe in SN 2023xgo (shown in the left inset of Fig. 3). The two peaks are not well resolved for SN 2023xgo, but can be seen clearly for the other SNe IIn, Ibn and SN 2023emq. These signatures in this phase are typical for young flash ionized SNe (D. Khazov et al. 2016; R. J. Bruch et al. 2021, 2023). SNe Icn at similar phases do not show a prominent flash ionized signature of these lines, however D. A. Perley et al. (2022) highlighted this as a 'narrow phase' for Type Icn SN 2021csp where a P-Cygni feature can be seen at similar wavelengths. SN 2023xgo also shows a prominent emission around 5700 Å due to C III λ5696. A very faint trace of that line is seen for SNe 2019uo, 2019wep, and the H-rich SN 1998S, but not prominent in SN 2010al, possibly due to comparison with an earlier phase spectrum. I. Shivvers et al. (2016) also noticed a line at 5700 Å in the early spectrum of the Type Ibn SN 2015U, in addition to the blended line at 4650 Å. They suggested that the line possibly arises from N II λ5680 because of the presence of more N II lines in their subsequent spectra. The C III λ5696 is one of the most prominent lines in our SN Icn sample. Fig. 3 shows that SN 2023xgo displays the most prominent C III λ5696 line among SNe Ibn, even more prominent than SN 2023emq, which also clearly showed this line but with less strength.

Although M. Pursiainen et al. (2023) argue that the flash ionization signatures could possibly arise for both SNe Ibn and SNe Icn, the presence of long-lasting C III λ5696 signatures in the spectral evolution of SN 2023xgo as compared with other SNe Ibn makes it different, which is probably a combined effect of ionization, abundance, density, and luminosity. A closer look at the feature at 4650 Å shows that the He II peak for SNe Ibn is more prominent than for SNe Icn, which was also noticed by C. Pellegrino et al. (2022b). SN 2023xgo shows a more symmetric, blended He II and C III/N III feature. Although the line at 5696 Å can be reasonably well reproduced by N II λ5680, we do not see evidence for other N II lines

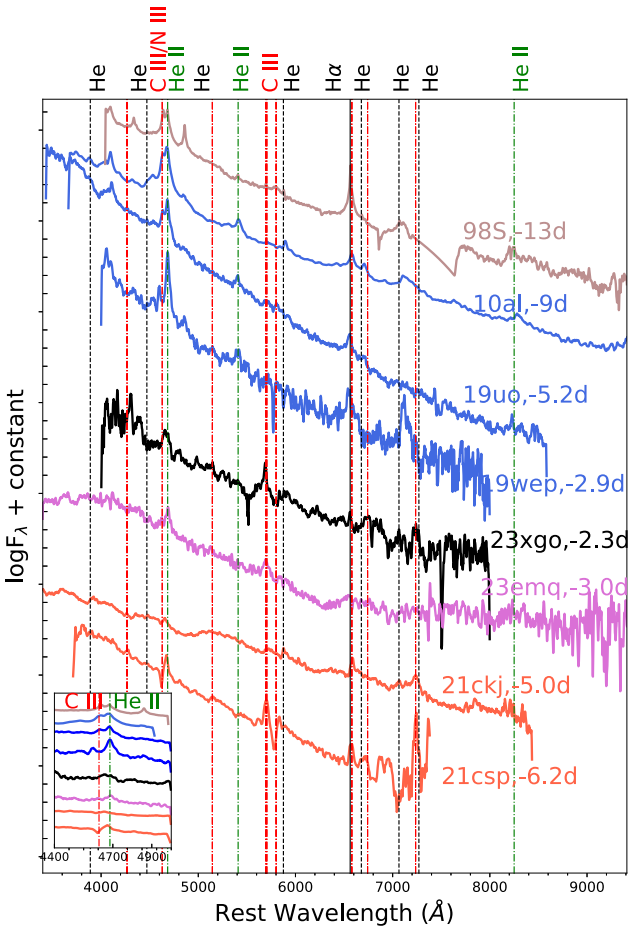

Figure 3. The early spectral comparison of SN 2023xgo (in black) with a selected sample of SNe. The insets mark the unique characteristics of SN 2023xgo, where it shows C III λ5696 as the most prominent feature in the spectral evolution, unlike other SNe Ibn with flash ionization signatures. The different colour coding are: Brown: Type IIn SNe; Blue: Ibn; Red: Icn, and Purple: transitional.

in the spectra. In this regard, SN 2023xgo seems more similar to SNe Icn, with stronger emission of C III λ5696 than SN 2023emq.

We measure the pseudo-equivalent width (EW) of the C III λ5696 feature for SN 2023xgo at −2.35 and −0.82 d past maximum (see Fig. 4). The estimated values are 40 ± 5 and 25 ± 5 Å. The pseudo-EW of the emission line for SN 2023xgo at this phase matches very well with the pseudo-EW measurements for SNe Icn 2019hgp and 2021csp. In contrast, the pseudo-EWs of C III for both SNe Ibn 2023emq and 2015U at similar phases are lower, at approximately 11 Å. The prominence of this line could be the result of a combination of high ionization conditions, carbon abundance, and elevated temperatures and densities in the emitting region. At this phase, SN 2023xgo shows similarity with SNe Icn.

3.1.1 Comparing the flash ionized spectrum with Boain and Groh models

Fig. 5 shows the comparison of the early time spectra of SN 2023xgo with a set of models by I. Boian & J. H. Groh (2019). They use the radiative transfer code CMFGEN to build an extensive library of spectra simulating the interaction of SN ejecta with their progenitor's wind or CSM. A range of progenitor mass-loss rates ($\dot{M} = 5 \times 10^{-4}$–$10^{-2}$

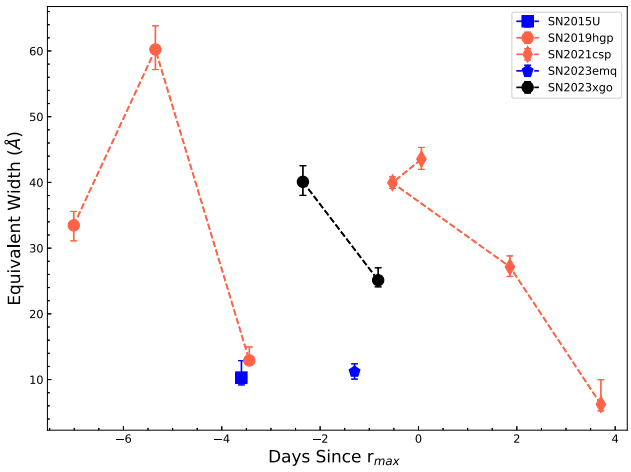

Figure 4. Pseudo-Equivalent Width measurements of C III λ5696 for a group of SNe Ibn and SNe Icn compared to the values measured for SN 2023xgo. The equivalent width values of SN 2023xgo show similarity with those of SNe Icn from the comparison sample. The red and the blue colours represent the SNe Icn and SNe Ibn, respectively.

$M_\odot$ yr^{-1}), abundances (solar, CNO-processed, and He-rich), and SN luminosities ($L = 1.9 \times 10^8 - 2.5 \times 10^{10}$ $L_\odot$) were considered in these models. The models simulate events approximately one day after explosion, and assume a fixed location of the shock front at $R_{in} = 8.6 \times 10^{13}$ cm. We have continuum-normalized our earliest spectrum (−2.35 d) and convolved it with the resolution of the available models ($R \sim 1000$). The left panel of Fig. 5 shows that the C III/N III, the He II features and the He II/H are well reproduced around 4600 and 6500 Å assuming a luminosity of 1.5×10^9 $L_\odot$, a mass-loss rate of 10^{-3} $M_\odot$ yr^{-1}, radius of 16×10^{13} cm, and solar abundance. Since H is absent throughout the spectral evolution of SN 2023xgo, the feature at 6500 Å is most likely due to He II. This gives us good confidence in our line identifications. However, these set of values do not reproduce the strength of the C III λ5696 feature, which is stronger than in the model. When we tried to match our spectrum with the higher luminosity model of $L = 3.1 \times 10^9$ $L_\odot$, a mass-loss rate of 3×10^{-3} $M_\odot$ yr^{-1} and radius of 32×10^{13} cm, the strength of the C III λ5696 is well reproduced, but all other flash ionized lines are overestimated. The luminosity at which we underestimate the C III λ5696 feature matches with our observed bolometric luminosity at this phase ($L = 5.22 \times 10^{42}$ erg s^{-1}). Although a stronger C III λ5696 profile might suggest a luminosity effect, luminosity is most likely not the primary driver here, as this SN is the least luminous in the Ibn/Icn sample (see Section 5). Instead, factors such as ionization, temperature, and density that themselves influence luminosity play a more significant role in shaping the observed carbon feature.

We want to remark that the models do not have radiation hydrodynamics that is post-processed by CMFGEN, so they assume a temperature of the radiation field and calculate the spectrum between R_{in} and R_{out} for a fixed shock velocity. So, the radius values can vary up to two orders in real time-scale. However, these models typically give us a mass-loss rate of 10^{-3} $M_\odot$ yr^{-1} for SN 2023xgo.

3.2 Post-maximum spectral evolution

Around maximum light, from 0.53 to 4.75 d in observer frame, we see narrow P-Cygni lines of He I λ5876 persisting in the spectral evolution of SN 2023xgo. Narrow P-Cygni He I λ5876 lines are a common feature seen in many SNe Ibn (G. Hosseinzadeh et al. 2017). In addition, He Iλλ6678,7065 start appearing at 4.75 d. From 5.34 d to about 10.97 d, the spectra show a transformation from narrow P-Cygni He I λ5876 to an intermediate width feature. During this phase, the features of Ca II, Si II, and Na ID also start appearing in the spectral evolution of SN 2023xgo (see Fig. 2).

Fig. 6 shows the spectral comparison, after maximum, of SN 2023xgo with a number of SNe Ibn (marked in blue) and SNe Icn (marked in red). The comparison sample is similar to the one used in Fig. 3 complemented with other spectra of SNe Ibn from G. Hosseinzadeh et al. (2017). The middle epoch comparison with SNe Ibn and Icn shows that SN 2023xgo has developed narrow P-Cygni feature of He I λ5876 at this phase, similar to SN 2019uo. The prominent lines of carbon have vanished during this phase. Although some very narrow helium is noticed for all the SNe Icn, it is much more significant in all SNe Ibn, as shown in the right zoomed-in panel of Fig. 6. Following the suggestion by G. Hosseinzadeh et al. (2017), the line evolution of SN 2023xgo shows that it belongs to the 'P-Cygni' subclass in the same way as SN 2019uo. The P-Cygni He I features are narrow but gradually broaden over time. The physical explanation could possibly be that an optically thick shell is lit up by the explosion, and the narrow P-Cygni features transition to broader emission as the shell is swept up by the SN ejecta. According to G. Hosseinzadeh et al. (2017), this is mostly an effect of the optical

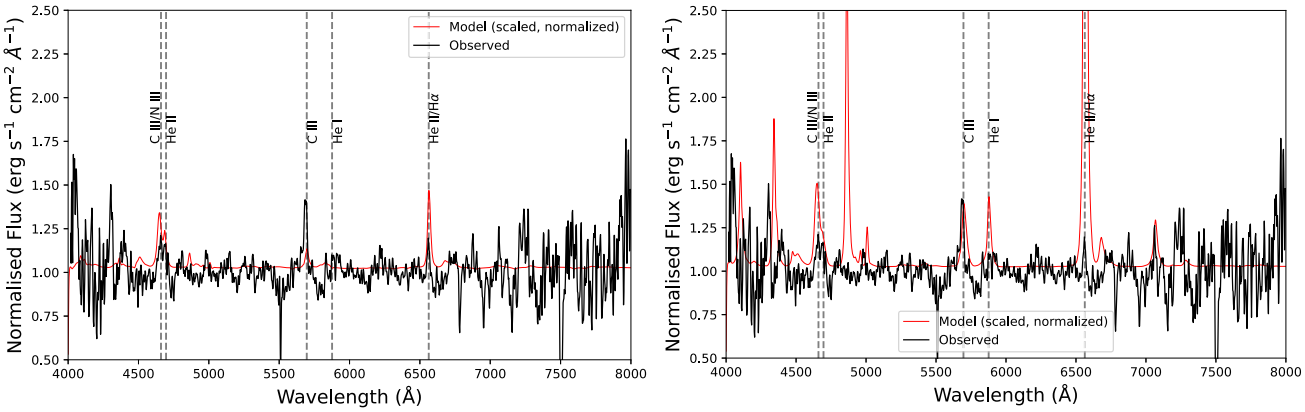

Figure 5. Comparisons of the earliest spectrum having flash ionization signatures of SN 2023xgo with models by I. Boian & J. H. Groh (2019). These are a set of radiative transfer codes (CMFGEN) which generate a set of spectra over different luminosity and mass-loss rates 1 d after explosion. Our spectra are reproduced by spectral model of mass-loss rate 10^{-3} $M_\odot$ yr^{-1} and increase in flux reproduces the C III λ5696 feature.

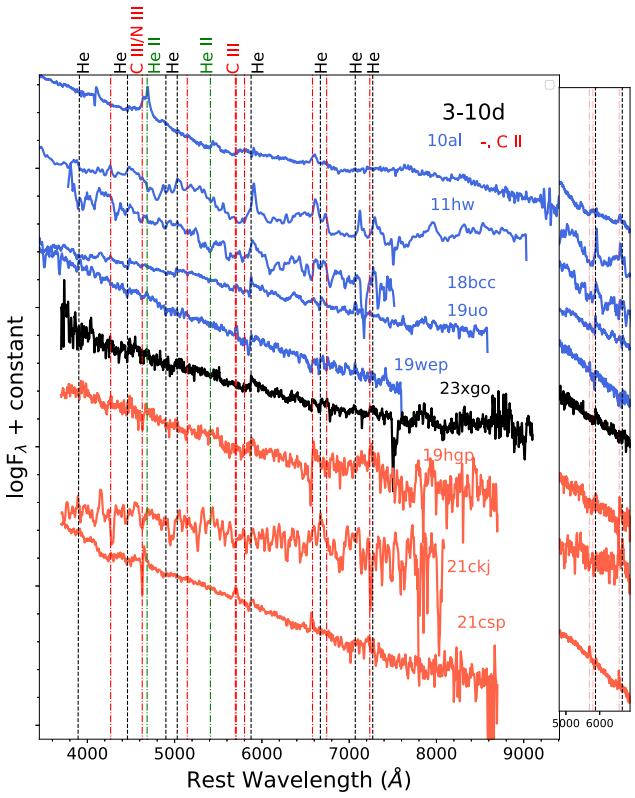

Figure 6. The mid epoch (3 − 10 d) spectral evolution of SN 2023xgo, compared with a set of SNe Ibn (blue) and SNe Icn (red). The right panel of the figure shows the inset region of the 5000 to 6000 Å region where we could detect both the 'P-Cygni' and 'emission' sub-class of He I λ5876.

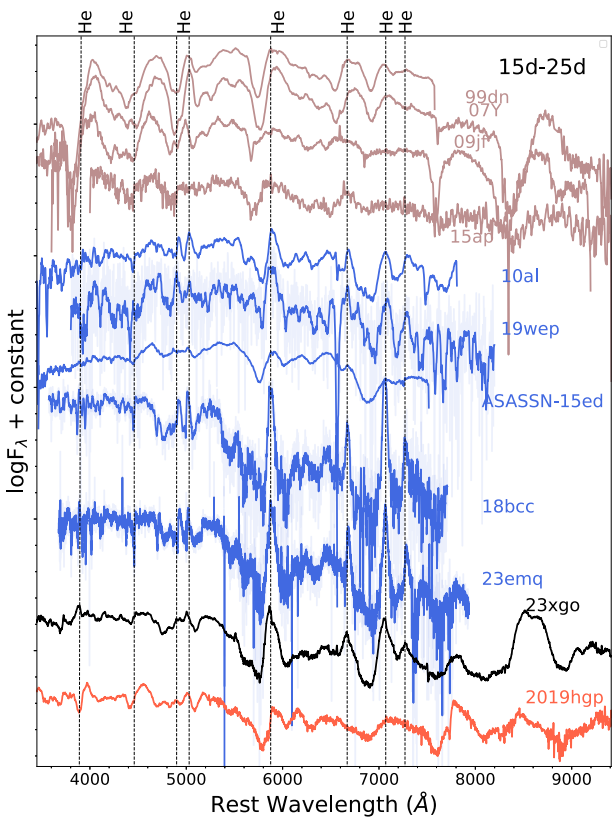

Figure 7. The late epoch (23.48 d) spectral comparison of SN 2023xgo with a group of SNe Ibn (blue), Icn (red), and Ib (brown). SN 2023xgo shows striking similarity with ASASSN-15ed at this phase, with broad P-Cygni features, and is also similar to some SNe Ib.

depth giving rise to both the P-Cygni and emission line profiles for SNe Ibn. The viewing angle dependence also determines whether a profile looks like 'P-Cygni' or 'emission', depending on whether it is viewed edge on or face on, which is not relevant if we already have an approximation of spherical symmetry. However, this scenario was questioned by E. Karamehmetoglu et al. (2021), who suggest that the line formation is instead largely dependent on the density, temperature, and optical depths. In their spectral modelling of SN Ibn 2018bcc (also shown in Fig. 6), they found that their observed profiles are a mix of both P-Cygni and emission profiles of helium as a result of high optical depths and densities in the CSM. They found that at late times, the emission lines of helium are still optically thick, but they are emission dominated because they lack other lines to branch into it. Helium ionization and recombination are mostly caused by UV and X-ray emission, occurring at the shock boundary deep in the interacting regions. Although most of the emission and the electron scattering are produced by the ionized region outside the shock, P-Cygni features usually originate from optical depths ≤ 1. X-rays penetrating further into the P-Cygni producing regions will fill in the absorption and lead to emission features. Thus, this provides an alternative scenario to the spectral profiles. This marks the phase when SN 2023xgo has transformed from a SN Icn to a SN Ibn with prominent lines of He I.

3.3 Late-time evolution

From 10.97 d to 23.48 d, the spectra of SN 2023xgo transform, and the He I features have developed significantly (see Fig. 7). Apart from the He I λλ5876, 6678 and 7065 features, some ejecta lines like the Ca NIR triplet are also seen in the spectral evolution of SN 2023xgo at this phase (see Fig. 2). Fig. 7 shows the comparison of SN 2023xgo with a group of SNe Ibn (blue), SNe Icn (red), and SNe Ib (brown), at late epochs. The spectral evolution of SN 2023xgo shows remarkable similarity with ASASSN-15ed, which had full width at half maxima (FWHM) velocities of the He I λ5876 line in the order of 5000 − 6000 km s^{-1}, whereas the FWHM velocity for SN 2023xgo is 6300 ± 1000 km s^{-1}. This is less than the typical velocity for SNe Ib which have absorption trough velocities between 7000 − 9000 km s^{-1}, as seen in the brown-coloured spectra of our comparison sample (Fig. 7). For the other SNe Ibn (2010al, 2018bcc, 2019wep, and 2023emq), we do see absorption dips for He I λ5876, but less prominent than for SN 2023xgo. It is interesting to note that SN 2019hgp, which is a SN Icn, also shows a similar absorption profile at 5800 Å as the helium feature in SNe Ibn, but for the SN Icn this is most likely due to an adjacent C II line. The major difference observed between SN Ibn and SN Ib spectra is that SNe Ibn have more symmetric line profiles, while in SNe Ib the absorption part dominates over the emission. We note that, the absorption components of the He I lines in SN 2023xgo are similar to those in SN Ib spectra, suggesting a higher kinetic energy per mass unit in the SN ejecta. This is seen especially in the late phases of SNe Ibn that develop broad lines (A. Pastorello et al. 2015c). The simultaneous presence of a very narrow feature at early phases and a transition to broader features later on suggests that these features arise from different emitting regions: the broader He I P-Cygni features are likely a signature of the SN ejecta, while the

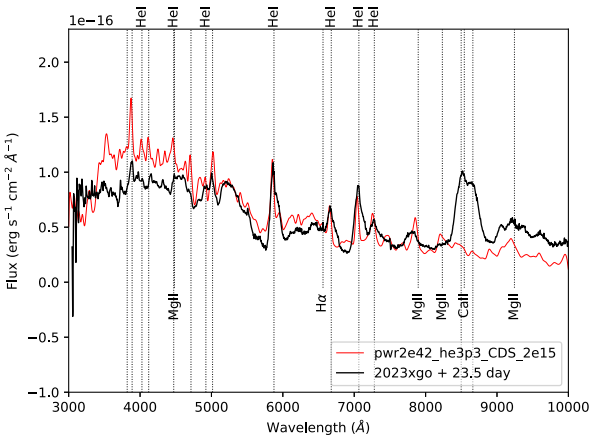

Figure 8. The best match of our observed (23.48 d) spectrum with the models by L. Dessart et al. (2022). We find that a low mass He star model of 3 $M_\odot$ best reproduces our observed He I spectral features.

narrow He I P-Cygni lines are generated in the unperturbed, He-rich CSM.

3.3.1 Late phase spectral matching

To investigate the behaviour of SN 2023xgo during the nebular phases, we compare our last epoch spectrum (23.48 d) with a set of nebular phase spectral models by L. Dessart, D. J. Hillier & H. Kuncarayakti (2022), who performed numerical simulations for radiation hydrodynamics of the ejecta and CSM as well as non-local thermodynamic equilibrium (non-LTE) radiative transfer in a H-free, He-rich dense shell powered by interaction. We compare the last spectrum of SN 2023xgo with the models by L. Dessart et al. (2022), both for binary and single He star explosion models, with the mass of the star ranging between 2.9 $M_\odot$ and 12 $M_\odot$, and assuming two shells corresponding to ejecta and CSM, respectively, taken from the models by T. Ertl et al. (2020). Comparing with a grid of He-star mass models having a CDS velocity of 2000 km s^{-1}, a grid of luminosity between $2 - 10 \times 10^{42}$ erg s^{-1} and different mixing, we find the best fit match with a model of 3 $M_\odot$ He star. The best-matched model spectrum (Fig. 8) has a luminosity of 2×10^{42} erg s^{-1}, higher than our observed bolometric luminosity of 6.0×10^{41} erg s^{-1} at similar phases. We applied Gaussian smoothing to match the model resolution to the spectral resolution of our data. The prominent He I lines at λλ4471, 5876, 6678, 7065, and 7281 are well reproduced. The model also captures several O, Si, and Mg emission features across the optical range. Despite strong emission in the blue, this region is heavily suppressed by Fe line blanketing (L. Dessart et al. 2022). Some of the Mg lines are well matched, while Ca is underestimated, possibly due to differences in the structure of the density of CDS influenced by turbulence, temperature and ionization, as seen also in SN 2006jc (L. Dessart et al. 2022). The mismatch also reflects uncertainties in the progenitor shell compositions. L. Dessart et al. (2022) have shown that Mg emission dominates in the ONeMg shells, whereas Ca dominates in the Si/S and Fe/He shells. Thus, O I, Mg II, and Ca II line strengths are highly model dependent, distinguishing interacting SNe from normal Type Ibc models. Overall, the observed He features are consistent with those in the model of a 3 $M_\odot$ He star with a CDS at 2×10^{15} cm. In contrast, SN 2020nxt showed a late-time increase in the Ca II NIR triplet strength as the shell ionization dropped (Z. Y. Wang et al. 2024), an effect not captured in L. Dessart et al. (2022), suggesting an ionization rather than abundance origin. Notably, the models by L. Dessart et al. (2022) overpredict flux of the Mg II lines at 7896, 8234, and 9218 Å at all epochs, which we do not observe prominently in our spectra.

3.4 Velocities and pseudo-equivalent width evolution

Fig. 9 shows the pseudo-EW and the velocity evolution of three helium lines in the spectra of SN 2023xgo, compared with the measurements from other members of the SN Ibn sample from G. Hosseinzadeh et al. (2017). We see that the velocities and pseudo-EWs for SN 2023xgo increase drastically for all He I lines. The emission lines of He I were fit using a Gaussian on a linear continuum. The estimates of the pseudo-EW involve the calculation of the integral of the flux normalized to the local continuum. In this estimate, we do not measure the pseudo-EW of the absorption component of the P-Cygni lines. The velocities are estimated from the FWHM of the emission component of the He I profile. We see an increasing trend in both the line velocities and pseudo-EWs of the He lines. The velocity estimates of SN 2023xgo lie at the upper range of what is found for SNe Ibn and show a faster evolution. In SN 2023xgo, the broad features seen are wider than typical emission velocities for SNe Ibn around maxima. The FWHM velocity of He I λ5876 for SN 2023xgo is much broader than most of the SNe Ibn of our comparison sample. It is important to note that the measured FWHM of He I λ5876 may be affected by contamination from Na I D, particularly at certain phases, which could influence the line width measurements. In our comparison sample, ASASSN-15ed and SN 2019wep lie in the higher velocity end of SNe Ibn; however, SN 2023xgo shows an even higher FWHM velocity at later phases. G. Hosseinzadeh et al. (2017) claimed that the 'P-Cygni' subclass showed a faster evolution in line velocities reaching broader emission profiles while the emission subclass shows less evolution in line velocities. The pseudo-EWs of the He I lines for SN 2023xgo are at an the very high end compared to the normal SNe Ibn. This indicates that the late time behaviour of SN 2023xgo is similar to what is seen in SNe Ibn, which shows ejecta signatures at late phases reaching velocities of almost the same high velocities as SN Ib do at this phase.

4 HOST GALAXY

4.1 Observations

We retrieved science-ready coadded images from the Panoramic Survey Telescope and Rapid Response System (Pan-STARRS, PS1) DR1 (K. C. Chambers & Pan-STARRS Team 2016), the Two Micron All Sky Survey (2MASS; M. F. Skrutskie et al. 2006), and *WISE* images (E. L. Wright et al. 2010) from the unWISE archive (D. Lang 2014).[10] that include *WISE* data from the NEOWISE-Reactivation mission 1 − 7 (A. Mainzer et al. 2014; A. M. Meisner, D. Lang & D. J. Schlegel 2017). We used the software package LAMBDAR (Lambda Adaptive Multi-Band Deblending Algorithm in R) (A. H. Wright et al. 2016) and tools presented in S. Schulze et al. (2021), to measure the brightness of the host Galaxy. To expand the spectral energy distribution (SED) we use the *Swift* data obtained between December 2023 and January 2024 and measured the brightness using a slightly larger aperture than in the optical to account for differences in the point spread function. All measurements are summarized in Table 1. We also observed the host Galaxy spectrum of the SN using KCWI. The observations made on 2024 August 10, and 2025 January

[10] http://unwise.me

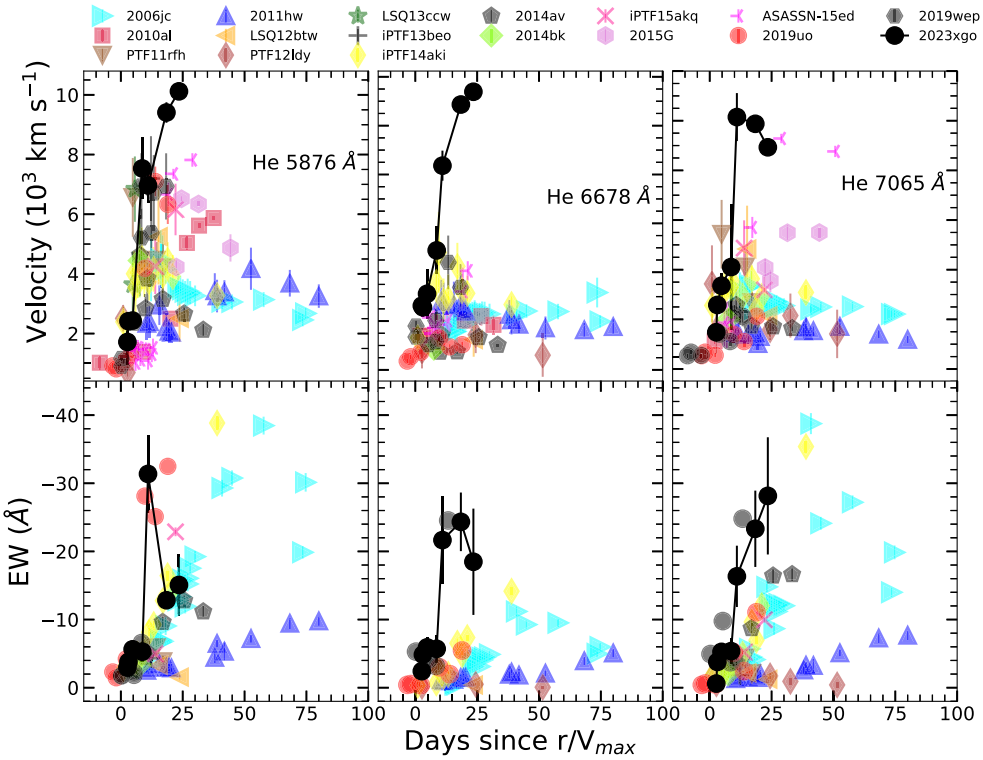

Figure 9. The velocity and equivalent widths of the He I λλ5876, 6678 and 7065 lines of SN 2023xgo compared with the values from a group of SNe Ibn from G. Hosseinzadeh et al. (2017).

Table 1. Photometry of the host Galaxy of SN 2023xgo.

Survey/ Telescope	Instrument	Filter	Brightness (mag)
Swift	UVOT	$w2$	20.49 ± 0.12
Swift	UVOT	$m2$	20.58 ± 0.14
Swift	UVOT	$w1$	19.86 ± 0.17
Swift	UVOT	u	18.85 ± 0.17
Swift	UVOT	v	16.96 ± 0.13
PS1	–	g	17.36 ± 0.04
PS1	–	r	16.79 ± 0.05
PS1	–	i	16.49 ± 0.04
PS1	–	z	16.30 ± 0.04
PS1	–	y	16.11 ± 0.10
2MASS	–	J	16.00 ± 0.07
2MASS	–	H	15.78 ± 0.10
WISE	–	$W1$	16.91 ± 0.09
WISE	–	$W2$	17.53 ± 0.07

Note. All magnitudes are reported in the AB system and are not corrected for reddening.

1. The original observations were reduced using the official pipeline. Cosmic ray rejection was performed using a modified version of the KcwiKit pipeline,[11] sky background subtraction was done with ZAP and inverse sensitivity and telluric fitting were handled with KSkyWizard.[12] The frames were then stacked using an inverse-variance weighted average. The elliptical aperture is defined using one-sigma isophotal fitting from photutils, and the host spectra were extracted using aperture sizes of 1×, 1.5×, and 2× the fitted size.

4.2 Spectral energy distribution modelling

We model the observed SED with the software package `Prospector` (B. D. Johnson et al. 2021) version 1.4.[13] We assume a Chabrier initial-mass function (IMF; G. Chabrier 2003) and approximate the star-formation history (SFH) by a linearly increasing SFH at early times followed by an exponential decline at late times. To account for any reddening between the expected and the observed SED, we use the Calzetti attenuation model (D. Calzetti et al. 2000). The priors of the model parameters are set identical to those used by S. Schulze et al. (2021).

Fig. 10 shows the observed SED and its best fit. The SED is adequately described by a Galaxy template with a mass of $10^{9.31^{+0.13}_{-0.22}}$ $M_\odot$, and a star-formation rate of $0.05^{+0.02}_{-0.01}$ $M_\odot$ yr^{-1}. The mass and star-formation rate are similar to those of the SN host galaxies from the Palomar Transient Factory (grey contours; S. Schulze et al. 2021), SNe Ibn and SNe Icn (colour-coded; the values of the SNe Icn were taken from A. Gal-Yam et al. 2014; D. A. Perley et al. 2022; C. Pellegrino et al. 2022b).

[11] https://github.com/yuguangchen1/KcwiKit
[12] https://github.com/zhuyunz/KSkyWizard

[13] `Prospector` uses the `Flexible Stellar Population Synthesis` (`FSPS`) code (C. Conroy, J. E. Gunn & M. White 2009) to generate the underlying physical model and `python-fsps` (D. Foreman-Mackey, J. Sick & B. Johnson 2014) to interface with `FSPS` in `python`. The `FSPS` code also accounts for the contribution from the diffuse gas based on the `Cloudy` models from N. Byler et al. (2017). We use the dynamic nested sampling package `dynesty` (J. S. Speagle 2020) to sample the posterior probability.

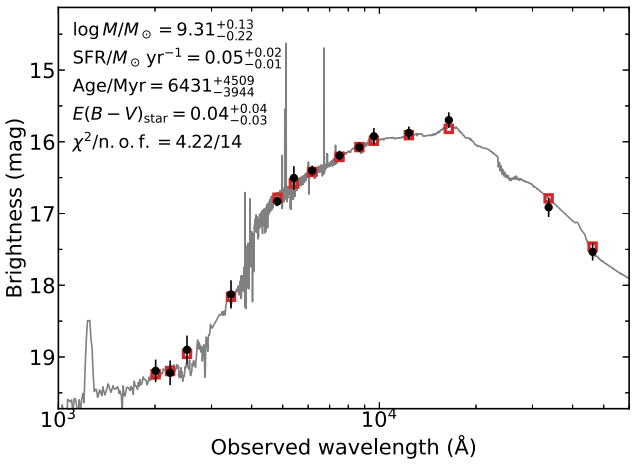

Figure 10. Spectral energy distribution (SED) of the host Galaxy of SN 2023xgo from 1000 to 60 000 Å (black data points). The solid line displays the best-fitting model of the SED. The red squares represent the model-predicted magnitudes. The fitting parameters are shown in the upper-left corner. The abbreviation 'n.o.f'. stands for number of filters.

Table 2. Emission line fluxes measured from the host Galaxy spectrum of SN 2023xgo.

Line	Flux (10^{-16} erg cm^{-2} s^{-1})
[O III] λ4960	18.81 ± 0.94
[O III] λ5007	59.10 ± 1.59
Hγ	8.82 ± 1.27
Hβ	35.48 ± 5.45
Hα	126.95 ± 2.80
[N II] λ6549	6.24 ± 1.01
[N II] λ6585	17.39 ± 1.18

After tying the flux calibration of the host spectra to the host photometry, we could measure the line fluxes from a simple emission line analysis, measuring the line fluxes of [O III] λ4960, 5007, Hα, Hβ, and [N II] λ6549, 6585 lines reported in Table 2. The values reported are not corrected for extinction.

The MW-extinction corrected Hβ/Hα flux ratios are ≈ 3.6, differing from the theoretically predicted value of 2.86, assuming Case B recombination, electron temperature of 10^4 K, and electron density of 10^2 cm^{-3} (D. E. Osterbrock & G. J. Ferland 2006). The excess in the flux ratio translates to $E_{\mathrm{host}}(B-V) = 0.06^{+0.13}_{-0.06}$ mag, assuming the Calzetti attenuation model with $R_V = 4.05$. Using this O3N2 diagnostic together with the parametrization from M. Curti et al. (2017), we infer a gas-phase metallicity of 0.7 ± 0.1 solar. The Hα luminosity and the level of star formation are tightly correlated R. C. J. Kennicutt (1998). The attenuation-corrected star-formation rate is $0.05 \pm 0.02\ \mathrm{M}_\odot\ \mathrm{yr}^{-1}$ using R. C. J. Kennicutt (1998) and P. Madau & M. Dickinson (2014) to convert from the Salpeter IMF (assumed in R. C. J. Kennicutt 1998) to the Chabrier IMF (assumed in our Galaxy SED modelling).

The host Galaxy of SN 2023xgo is a low-mass ($\sim 10^{9.3}\,\mathrm{M}_\odot$), moderately star-forming ($\sim 0.05\,\mathrm{M}_\odot\ \mathrm{yr}^{-1}$), and subsolar-metallicity ($\sim 0.7\,\mathrm{Z}_\odot$) dwarf system. These characteristics closely match observed host environments of Type Ibn SNe that have been linked to interacting binary progenitors via observational and modeling studies (e.g. N.-C. Sun et al. 2019; Y.-J. Qin & A. Zabludoff 2024; Z. Y. Wang et al. 2024; T. J. Moriya et al. 2025). In particular, systems like SN 2006jc and SN 2015G show direct evidence for surviving companions in low-metallicity hosts, and population synthesis supports ultrastripped helium stars in compact binaries as plausible progenitors in such galaxies. A more pictorial representation of the SFR of SN 2023xgo with other SNe Ibn and Icn is shown in Fig. 11.

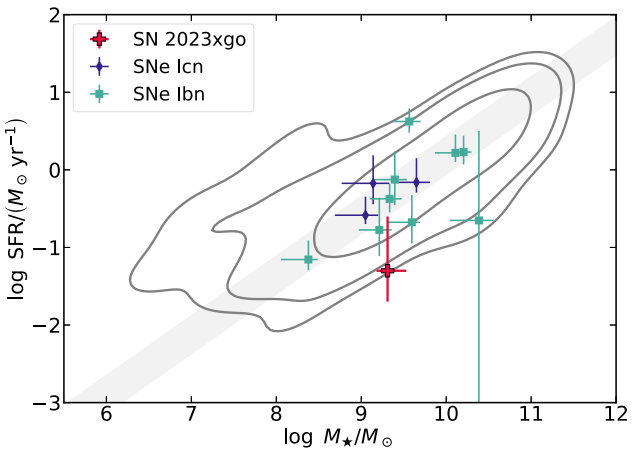

Figure 11. The host galaxies of SN 2023xgo and the other Type Ibn/Icn SNe in the context of all core-collapse SN host galaxies from the Palomar Transient Factory (PTF). The grey contours are data from PTF (S. Schulze et al. 2021), SNe Ibn and SNe Icn (colour-coded; the values of the SNe Icn were taken from A. Gal-Yam et al. 2014; D. A. Perley et al. 2022; C. Pellegrino et al. 2022b). The host of SN 2023xgo has fairly common properties for Type Ibn/Icn SNe.

5 PHOTOMETRIC EVOLUTION

The complete light-curve evolution of SN 2023xgo is shown in Fig. 12. Although we probably missed the peak in the UV light curves and other broad-band filters, we can trace the maxima in the *gri*-bands. The light curves of SN 2023xgo were observed in the near-infrared bands of *zJHK* as well. To estimate the peak date and magnitude, we use the Gaussian Process (GP) interpolation, utilizing the `PYTHON` package `GEORGE` (S. Ambikasaran et al. 2015) with a Matern 3/2 kernel (see Fig. 13). We used the interpolated *r*-band light curve to estimate the peak magnitude and to define the rise time as the time between the explosion epoch and the epoch of maximum. The *r*-band maximum is estimated to be MJD 60262.86 ± 0.46 at 16.43 ± 0.12 mag. Assuming the explosion epoch as inferred in Section 1.2, we find that the rise time of SN 2023xgo from explosion to maximum is 5.14 ± 2.30 d. This is well within the estimated values of rise times seen for a sample of SNe Ibn (G. Hosseinzadeh et al. 2017) and SNe Icn (C. Pellegrino et al. 2022b).

The *g* and *r*-band light curves between 0 and 30 d showed decline rates of 0.141 ± 0.003 and 0.139 ± 0.004 mag d^{-1}, respectively. The sample of SNe Ibn in G. Hosseinzadeh et al. (2017) are fast-evolving with a typical decline rate of 0.1 mag d^{-1} during the first month post-maximum. SN 2023xgo follows the same decay rate, but on the faster end of the distribution. We also notice a late-time flattening in all the light curves of SN 2023xgo, which is most likely due to a combination of CSM interaction and radioactivity (or some central powering source) contributing at late times.

Fig. 14 shows the absolute magnitude light curve of SN 2023xgo along with those of other SNe Ibn and Icn. The absolute magnitude of SN 2023xgo is -17.65 ± 0.04 mag (corrected for host and galactic extinction), making it one of the faintest members among the SN Ibn and SN Icn comparison sample used in the paper. It is also ∼1.9 mag fainter than the normalized SN Ibn light curve. The blue band in Fig.

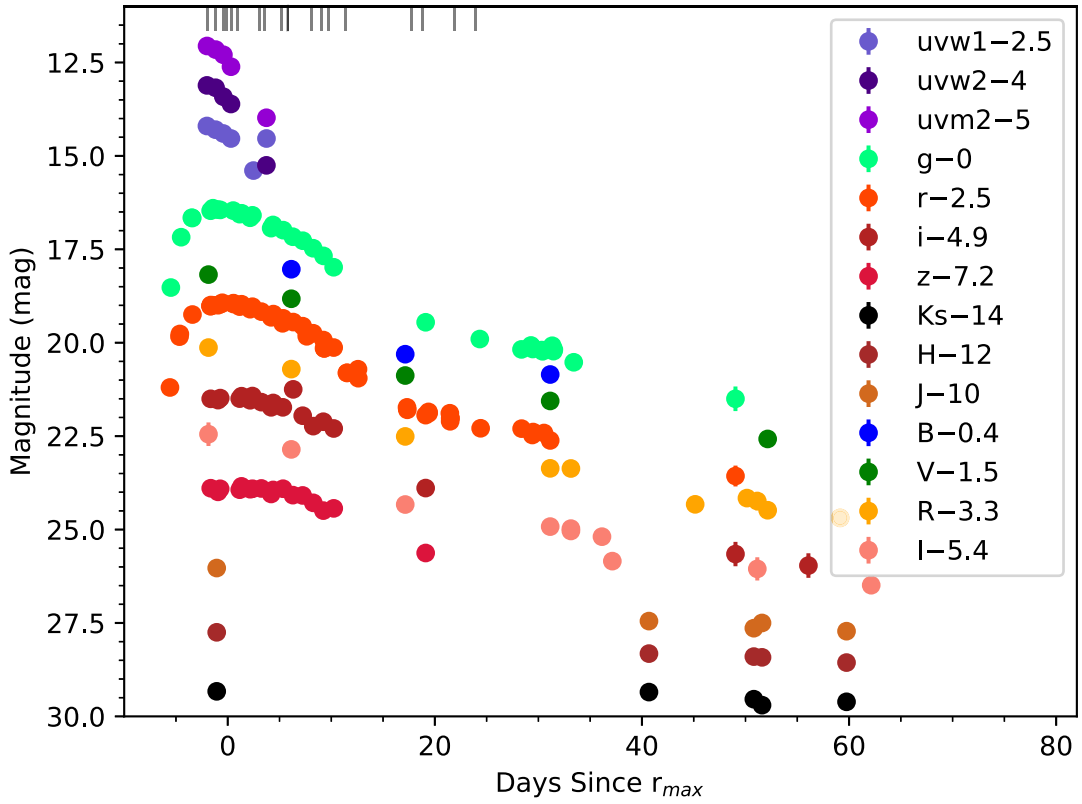

Figure 12. *uvBgVRIrizJHK* light-curve evolution of SN 2023xgo. The light curves show a fast early rise to peak, a decline consistent with those of most SNe Ibn, and then a flattening at late times. All magnitudes are plotted in AB. The vertical lines on top denote the phases at which spectra have been observed.

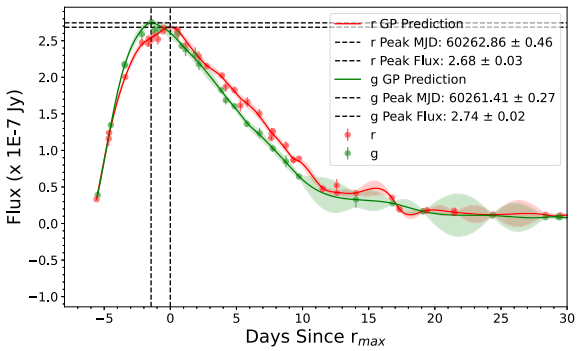

Figure 13. Figure shows the Gaussian process interpolation to estimate the time of maximum and the peak magnitude in g and r bands.

14 shows the average light curve (comprising 95 per cent of the SN Ibn data) taken from G. Hosseinzadeh et al. (2017). The average light curve was generated using a Gaussian process to fit a smooth curve to the combined light curves of the sample of G. Hosseinzadeh et al. (2017). The fit was performed in log–log space to ensure consistency and smoothness between the early and late-time light curves.

The lower panel of Fig. 14 shows the colour evolution of SN 2023xgo compared with all other SNe Ibn/Icn in the comparison sample. SN 2023xgo shows an initial blue-to-red transition in the colours. The $(g/B - R/r$-) colour evolution of SN 2023xgo increases from r-0.01 mag up to 0.59 mag ∼15 d post r-band max, subsequently remains flatter till ∼50 d. Even though the early colour evolution of SN 2023xgo is similar to most SNe Ibn, the trend in the colour evolution of SN 2023xgo at late phases is similar to that of SN 2019wep, which is a SN showing Ibn-like features early on but looks like SN Ib at later stages. The colour behaviour of SN 2023xgo is quite different from that of SN 2006jc, which shows a late-time flattening in the colour curve. All SNe Icn in our sample also show almost similar evolution in the colour as does SN 2023xgo.

Fast transients are a group of objects that rise and fade in brightness on time-scales much shorter than those of typical SNe (M. R. Drout et al. 2014; K. Maeda & T. J. Moriya 2022; C. Pellegrino et al. 2022b). The progenitor systems include massive WR stars undergoing core collapse, compact object mergers such as neutron star–black hole interactions, and ultrastripped SNe resulting from binary evolution. These scenarios reflect the diversity of mechanisms leading to rapidly evolving luminous events, and they display spectra with a featureless blue continuum similar to those of most SNe Ibn/Icn. A. Y. Q. Ho et al. (2023), using the sample of fast transients from ZTF, found an interesting connection between these fast transients and SNe Ibn/Icn. We therefore made the comparison of SNe Ibn with a group of fast transients. Fig. 15 shows the time-scales and luminosities of SNe Ibn/Icn and fast transients, where Δm_{15} (which is the decay rate from peak to 15 d post-maximum) and absolute magnitude are plotted against the rise time. The rise time, here, is calculated as the time between explosion and maximum light. The SNe for which explosion epochs are not constrained, we estimate the time as the difference between discovery and the maximum light, which gives a lower limit on the rise times typically. The plot indicates that the rise time of SN 2023xgo is longer than the fast transients but is well consistent with the rise time estimates of other SNe Ibn and SNe Icn. The Δm_{15} value matches well with SN 2014av and is on the higher end of SNe Ibn/Icn. Although rise times indicate that SN 2023xgo lies at the faster end of the SNe Ibn/Icn sample, still, the

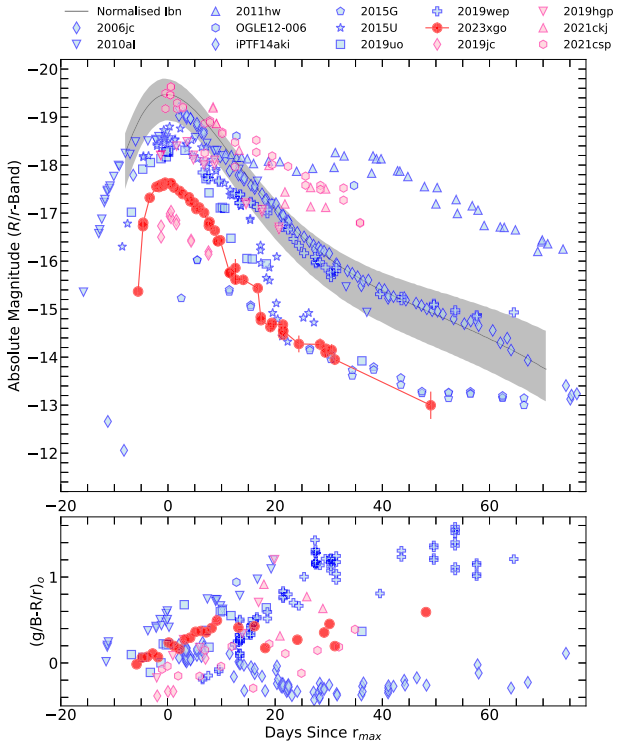

Figure 14. Upper panel of the Figure shows the *r*-band light curve comparison of SN 2023xgo with a sample of SNe Ibn (blue)(G. Hosseinzadeh et al. 2017). The SN Ibn comparison sample includes SNe 2006jc (R. J. Foley et al. (A. Pastorello et al. 2007; R. J. Foley et al. 2007), 2010al (A. Pastorello et al. 2015a), OGLE-SN-006 (A. Pastorello et al. 2015b), 2011hw (A. Pastorello et al. 2015a), iPTF14aki (G. Hosseinzadeh et al. 2017), 2015U (I. Shivvers et al. 2016; G. Hosseinzadeh et al. 2017), 2015G (G. Hosseinzadeh et al. 2017), 2019uo (A. Gangopadhyay et al. 2020) and 2019wep (A. Gangopadhyay et al. 2022). Phase is plotted in observer-frame days with respect to maxima for all the panels. The SN Icn sample (red) has been taken from D. A. Perley et al. (2022); C. Pellegrino et al. (2022b); T. Nagao et al. (2023). Lower panel shows the colour of SN 2023xgo plotted with the comparison sample.

most remarkable feature is still that it is among the faintest of our SNe Ibn/Icn comparison sample. In fact, SN 2023xgo is fainter than for most of the fast transients. SN 2023xgo, thus, stands out to be least luminous but fast decaying member of SNe Ibn/Icn among our comparison sample.

We also compare the time above the half-maximum with the peak absolute magnitudes for all the groups of SNe from the Bright Transient Survey sample taken from the BTS explorer (SNe IIn, IIb, Ib, Ic, Ibn, Icn; D. A. Perley et al. 2020) to see where it stands out in that space (see Fig. 16). Motivated by the fact that the SN 2023xgo shows a fast rise and decay observationally, and also shows low ejecta masses and Ni masses (from light-curve modelling; see Section 6), we also compare it with the sample of fast transients that could be ultrastripped from K. K. Das et al. (2024). SN 2023xgo also shows a very unique behaviour in this space. Even though it is less luminous than all the interacting SNe of our comparison sample, the time above maximum are similar to those of SNe Ibn/Icn except SN 2005la. SN 2023xgo is slower than most of the usual ultrastripped fast transients, but is faster than almost the entire stripped envelope population and most SNe IIn. This hints towards the possibility that even if the SN is powered by CSM interaction, the contribution of CSM is not as much as seen in other SNe Ibn, and it could also be a little bit of radioactivity contributing to the light curve of SN 2023xgo.

6 BOLOMETRIC AND MULTIBAND LIGHT-CURVE MODELLING

To construct the (pseudo-)bolometric light curve of SN 2023xgo from UV to IR, we used the `SuperBol` code (M. Nicholl 2018). The missing UV and NIR data were supplemented by extrapolating the SEDs using the blackbody approximation, and then we used the direct integration method as described in J. A. Lusk & E. Baron (2017). The UV extrapolation on the blue end was restricted up to a wavelength of 3000 Å.

Typically, as the SN ejecta expand, the shock breakout from the surface of the progenitor is followed by a rapid cooling phase due to the rapid expansion driven by the shock (S. W. Falk, J. M. Lattimer & S. H. Margolis 1977). This would lead to a increasing photospheric radius and a decrease in the temperature of the SN ejecta within a couple of hours of the explosion. However, for interacting SNe this is not always the case as the ejecta are masked by the CSM (I. Irani et al. 2024). Fig. 17 shows the radius and temperature evolution of SN 2023xgo. The temperature and radius are obtained from the blackbody fits, including the UV to NIR data. The Stefan–Boltzmann law was used to estimate the luminosity, temperature and radius. SN 2023xgo first shows a constant temperature varying between 14 500 and 15 500 K till maximum light. Following maximum light, the temperature declines to approximately 9500 K and subsequently remains roughly constant within the uncertainties. However, the increasing scatter and deviation from a smooth evolution suggest that the spectrum deviates from a simple blackbody approximation at these phases. The early high temperature indicates an injection of energy in the cooling ejecta, perhaps due to interaction with a dense CSM.

The blackbody radius of SN 2023xgo increases from approximately 6200 $R_\odot$ to 12 000 $R_\odot$ at maximum light. From maximum light until 24 d past maximum, the radius decreases from about 12 000 $R_\odot$ to 5000 $R_\odot$.

6.1 Semi-analytical modelling

While the decay of radioactive nickel synthesized in the explosion is the dominant powering mechanism for the light curves of most SESNe, that is not always the case for SNe Ibn. This is obvious for objects with extremely long-lived light curves (e.g. E. Karamehmetoglu et al. 2017; E. C. Kool et al. 2021), but is also generally true for the more luminous and rapidly evolving population (C. Pellegrino et al. 2022b; A. Y. Q. Ho et al. 2023). SN 2023xgo is, however, among the least luminous SNe Ibn/Icn, and therefore an investigation on how much radioactivity or interaction contributes to the overall light curve is warranted. We fitted the multiband light curves of SN 2023xgo with a suite of different models, to probe the powering mechanisms at play. The modelling was carried out with `REDBACK`, the Bayesian inference package for modelling transients (N. Sarin et al. 2024). In the subsequent modelling, we used a Gaussian likelihood. We fitted a CSM interaction-powered semi-analytic model (E. Chatzopoulos, J. C. Wheeler & J. Vinko 2012; E. Chatzopoulos et al. 2013), as well as a combination of that model with a radioactivity-powered analytic model (W. D. Arnett 1982). Each model was fitted to the entire photometric data set (UV/optical/IR), corrected for extinction using the estimated $A_V = 0.49 \pm 0.01$ mag (Section 1.3). We explored the parameter space with the nested sampling package `dynesty` (G. Ashton et al. 2019; J. S. Speagle 2020).

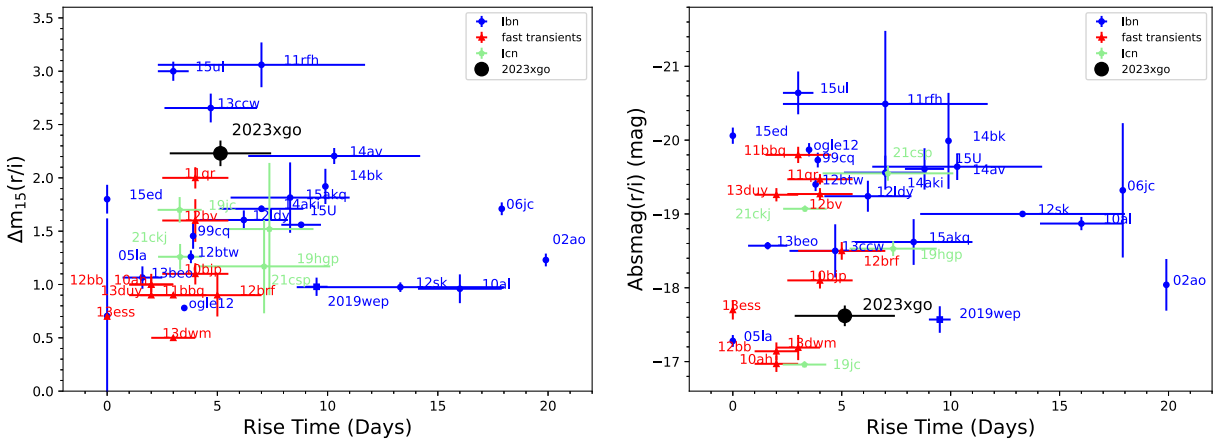

Figure 15. The Δm_{15} versus rise time (left panel) and absolute magnitude versus rise time (right panel) correlation plots of SN 2023xgo with a sample of SNe Ibn, Icn and fast transients. The sample of SNe Ibn is from G. Hosseinzadeh et al. (2017), the SNe Icn are taken from C. Pellegrino et al. (2022b), and the sample of fast transients is taken from M. R. Drout et al. (2014). The objects with '0' values, have possibly no estimation of rise times.

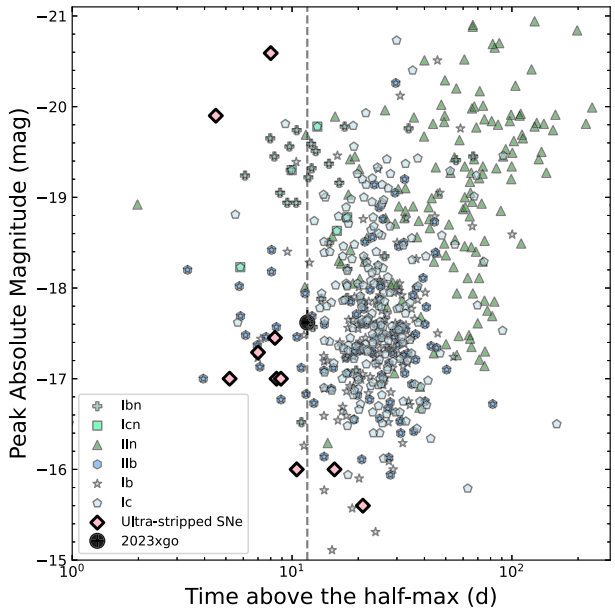

Figure 16. We compare the time above half maximum and peak absolute magnitude of SN 2023xgo with all other interacting and stripped-envelope SNe from the BTS experiment (D. A. Perley et al. 2020). For sources with two peaks in the *r*-band light curve, the second peak is used. We also compare SN 2023xgo with a group of fast-evolving transients that are thought to be ultrastripped SNe, and the comparison sample used is same as from K. K. Das et al. (2024). The dashed vertical line indicates SN 2023xgo in that phase-space.

6.1.1 *Radioactivity*

The main source driving the luminosity of a SN is often the radioactive decay of ^{56}Ni to ^{56}Co to ^{56}Fe. We started by assuming the radioactive decay of ^{56}Ni as the dominant source of energy. We fitted an W. D. Arnett (1982) model to the multiband light curves. The Arnett model assumes spherical symmetry and a homologous expansion of the ejecta. Table 3 contains the priors used for the inference. We fixed the optical (electron scattering), and gamma-ray opacities to the fiducial values of $\kappa_o = 0.07$ cm^2 g^{-1} (S. Valenti et al.

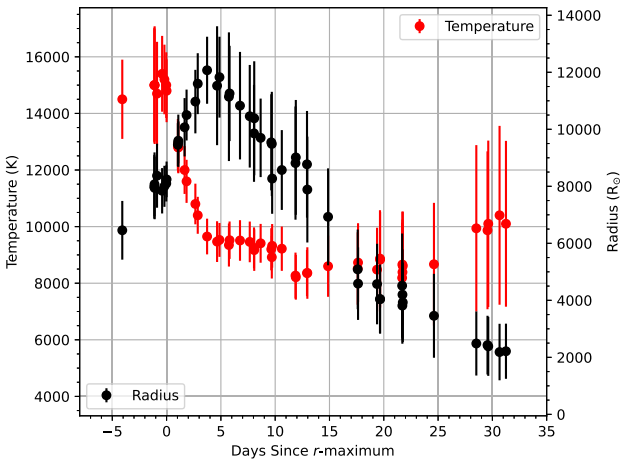

Figure 17. The radius and temperature evolution of SN 2023xgo. SN 2023xgo shows a temperature variation between 14 500 and 15 500 K, till maximum light, and then the temperature decreases to 9500 K and becomes flatter thereafter. The radius follows the same pattern as light-curve evolution with some phase offset, i.e. increasing to maximum light and decreasing thereafter.

Table 3. Table shows the best-fitting values obtained by fitting the equational form of W. D. Arnett (1982) assuming blackbody approximation. We see that radioactivity fairly reproduces our observed light curves in all the bands.

Parameters	Priors	Best fitted values
z	0.01325	0.01325
κ_o (cm^2 s^{-1})	0.07	0.07
κ_γ (cm^2 s^{-1})	0.03	0.03
$f_{\rm Ni}$	$\log\mathcal{U}$ [10^{-3}, 0.999]	$0.83^{+0.01}_{-0.01}$
$M_{\rm ej}$ ($M_\odot$)	$\log\mathcal{U}$ [0.25, 15]	$0.35^{+0.01}_{-0.01}$
$v_{\rm ej}$ (km s^{-1})	$\log\mathcal{U}$ [10^3, 5×10^4]	$17241.5^{+210.3}_{-206.5}$
$T_{\rm floor}$ (K)	$\log\mathcal{U}$ [10^3, 10^5]	$15215.8^{+56.7}_{-53.2}$
t_0 (MJD)	$\mathcal{U}$ [$t_{\rm detection}-70$, $t_{\rm detection}-1$]	$60255.81^{+0.02}_{-0.02}$

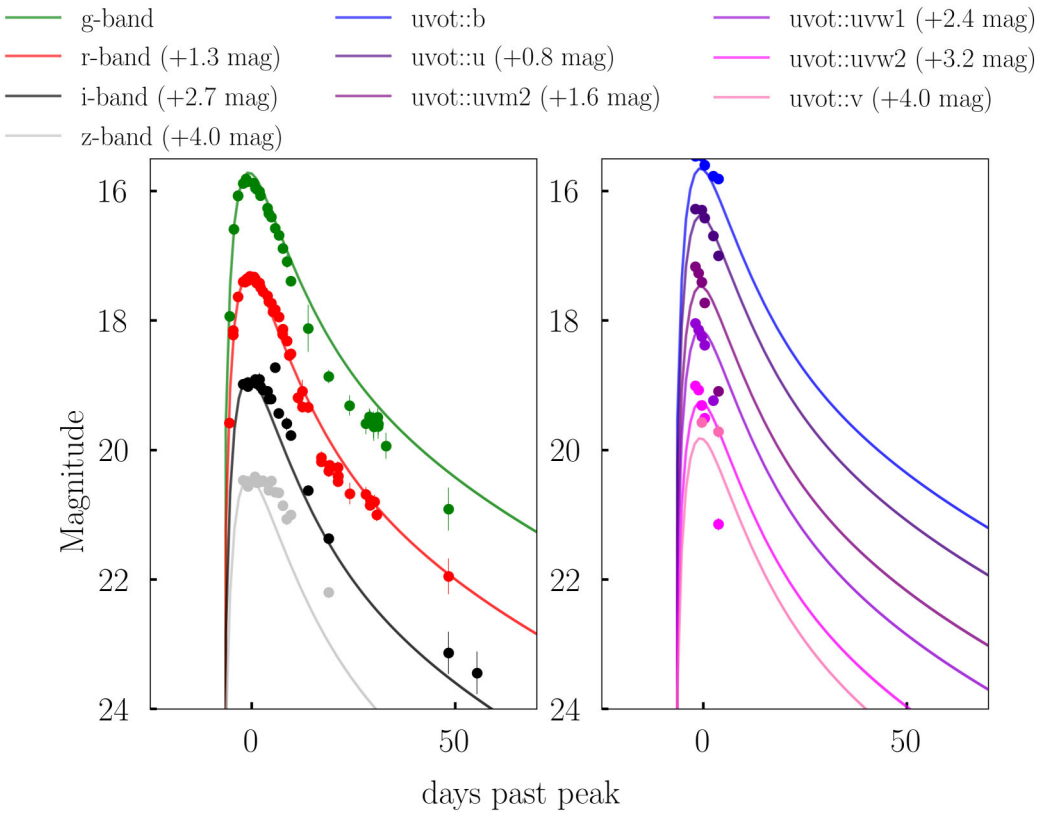

Figure 18. Multiband light-curve fitting of SN 2023xgo with radioactivity powered model by W. D. Arnett (1982) using REDBACK. We see that radioactivity fairly reproduces our observed light-curve evolution.

2008) and $\kappa_\gamma = 0.03$ cm^2 g^{-1} (S. A. Colgate & C. McKee 1969), respectively.

The free parameters of the ^{56}Ni model are the ejecta mass $M_{\rm ej}$ and the ^{56}Ni mass $M_{\rm Ni}$. Following W. D. Arnett (1982), τ_m determines the width of the bolometric light curve, which is also a free parameter and can be expressed in terms of the optical opacity κ_o, ejecta mass $M_{\rm ej}$, and the photospheric velocity at luminosity peak $v_{\rm ph}$:

$$\tau_m = \sqrt{2}\left(\frac{\kappa_o}{\beta c}\right)^{\frac{1}{2}}\left(\frac{M_{\rm ej}}{v_{\rm ph}}\right)^{\frac{1}{2}}, \quad (1)$$

where $\beta = 13.8$ is a constant of integration (W. D. Arnett 1982) and c is the speed of light. The kinetic energy for spherically symmetric ejecta with a uniform density is

$$E_k = \frac{3}{10} M_{\rm ej} v_{\rm ph}^2. \quad (2)$$

Fig. 18 shows the best-fitting Arnett model to the multiband light curves of SN 2023xgo and the cornet plot is shown in Fig. A1. It can account for the peak but slightly overestimates the decline rate. Nevertheless, the model of plain radioactive decay is good enough to approximate the entire light curve. Under the assumptions of the model, the inferred explosion parameters are listed in Table 3. The Arnett model yields an ejecta mass of $M_{\rm ej} \simeq 0.35$ M$_\odot$ with $M_{\rm Ni} \simeq 0.29$ M$_\odot$. A significant fraction of the ejected mass is thus required to be nickel (exceeding 50 per cent) for the Arnett model alone to reproduce the light curve. Although the multiband light curves are fairly well reproduced by this ^{56}Ni model, this very high fraction of nickel and the fact that we do see interaction signatures in the spectral evolution of SN 2023xgo make us consider other models. In particular, we also fitted a model with CSM-interaction in addition to radioactivity to the multiband light curves.

6.1.2 CSM

Since we wanted to infer whether our light curves are driven by CSM interaction only, we try to model our light curves with the semi-analytic model for CSM interaction from E. Chatzopoulos et al. (2012). We restricted the parameter space of our Bayesian inference in accordance with the following constraints: (i) the CSM photosphere would always be inside the CSM envelope and (ii) the diffusion time-scale would always be smaller than the shock crossing time-scale (two central assumptions in the work by E. Chatzopoulos et al. 2012).

In the `csm_interaction` model (the REDBACK implementation of the E. Chatzopoulos et al. 2012 treatment), it is assumed that the SN luminosity results from the conversion of kinetic energy from both the forward and reverse shock into heating. We fixed the opacity $\kappa_o = 0.07$ cm^2 g^{-1} and the gamma-ray opacity to $\kappa_\gamma = 0.03$ cm^2 g^{-1}. We take the rest of the parameters as fitting parameters.

For the ejecta mass (CSM mass), we consider uniform priors from 0.1 to 15 M$_\odot$ (0.001 − 15 M$_\odot$) based on the values obtained by C. Pellegrino et al. (2022a) for a sample of SNe Ibn. For the inner radius of the CSM (R_0), we consider a uniform prior from 0.1 to 100 AU, and for the CSM density at the inner radius (ρ), we consider a log-uniform prior for densities from 10^{-15} to 10^{-9} g cm^{-3}. The prior on the CSM density profile index, η, was chosen as a uniform distribution between $\eta = 0$ (shell-like) and $\eta = 2$ (wind-like).

The best-fitting parameters are listed in Table 4 and the best fit lightcurves are shown in Fig. 19. The 1σ errors listed represent only

Table 4. Table shows the best-fitting light-curve parameters from the CSM model.

Parameters	Priors	Best-fitting values
$M_{\rm ej}$ ($M_\odot$)	$\log\mathcal{U}$ [0.1, 15]	$1.0005^{+0.0001}_{-0.0001} \times 10^{-1}$
$v_{\rm ej}$ (km s^{-1})	$\log\mathcal{U}$ [10^3, 5×10^4]	$4966.2^{+7.1}_{-17.6}$
$M_{\rm CSM}$ ($M_\odot$)	$\log\mathcal{U}$ [0.001, 15]	$0.435^{+0.005}_{-0.001}$
$T_{\rm floor}$ (K)	$\log\mathcal{U}$ [10^2, 10^4]	$9971.3^{+22.2}_{-56.8}$
t_0 (MJD)	$\mathcal{U}$ [$t_{\rm detection} - 6$, $t_{\rm detection}$]	$60251.220^{+0.001}_{-0.001}$
η	$\mathcal{U}$ [0, 2]	$1.7^{+2.3}_{-1.2} \times 10^{-3}$
ρ (g cm^{-3})	$\log\mathcal{U}$ [10^{-15}, 10^{-9}]	$6.58^{+0.07}_{-0.04} \times 10^{-12}$
r_0 (AU)	$\log\mathcal{U}$ [10^{-1}, 10^2]	$1.01^{+0.01}_{-0.01} \times 10^{-1}$

the statistical uncertainty associated with the fitting and therefore are not indicative of the model uncertainties. It is important to note that some parameters (like $M_{\rm ej}$ and r_0) are 'pushing' the limits of the parameter space (see Table 4 and Fig. A2). The inference prefers a model with parameters outside the realistic ranges provided in the priors. Nevertheless, interpretation of the inferred parameters should be taken with caution in such cases.

We see that about 0.435 $M_\odot$ of CSM mass reproduces our observed light curves with an ejecta mass of 0.10 $M_\odot$ and a radius of CSM at 0.10 AU. Previous theoretical and observational studies of ultrastripped SNe have shown such low ejecta and CSM masses, as well as small CSM radii mostly for low-mass He stars in binary companion (S. C. Wu & J. Fuller 2022; K. K. Das et al. 2024)

The mass-loss rate estimated using the best fit parameters for our model is given by

$$\dot{M} = 4\pi R_{\rm CSM}^2 \rho_{\rm CSM} v_w, \tag{3}$$

where $\dot{M}$ is the mass-loss rate, $R_{\rm CSM}$ is the radius of the CSM, $\rho_{\rm CSM}$ is the density of the CSM, and v_w is the wind velocity. Using the values from Section 3.4, the $v_w = 1800$ km s^{-1} as measured from the spectrum around maximum light (see Subsection 3.4), the mass-loss rate is estimated to be 5.3×10^{-4} $M_\odot$ yr^{-1}. This is consistent with what we obtain by matching our values from the models of I. Boian & J. H. Groh (2019) in Subsection 3.1.1. The light-curve modelling favours a shell like scenario (see η from Table 4) here with shell expelled few hours before explosion. This time-scale is estimated from the radius and velocity listed in Table 4. Since this fit was not able to reproduce the late-time light-curve, and we see ejecta signatures start appearing in the spectra at 23.48 d, we further investigated whether radioactivity also plays a role in governing the light-curve evolution of SN 2023xgo.

6.1.3 CSM + Ni

Given the emergence of broad P-Cygni features in the spectral evolution of SN 2023xgo and the inability of a pure CSM interaction model to reproduce the late-time light curve, we adopted a hybrid approach combining the Arnett model (W. D. Arnett 1982) with the semi-analytic CSM interaction framework from E. Chatzopoulos et al. (2012). The Arnett model assumes that the main source driving the luminosity of a SN is the radioactive decay of ^{56}Ni to ^{56}Co to ^{56}Fe, assumes spherical symmetry, and a homologous expansion of the ejecta. Thus, along with the assumptions referred in Subsection 6.1.2, we included radioactivity as a powering source to reproduce the overall light curve of SN 2023xgo.

While fitting the combined radioactivity and the CSM interaction model, we find that when the data are fitted with prior parameters not restricted further than the fiducial ranges that they can take, the radioactive model dominates the luminosity output. We therefore decided to constrain $M_{\rm Ni}$ to allow for some appreciable contribution from the E. Chatzopoulos et al. (2012) model. We assumed that $M_{\rm Ni}$ cannot take values larger than 0.04 $M_\odot$, motivated by the typical values of $M_{\rm Ni}$ reported for the sample of C. Pellegrino et al. (2022a). The chosen priors and the best-fitting values of the model's free parameters are listed in the second and third columns of Table 5, respectively.

We fitted the multiband light curves of SN 2023xgo with the `csm_nickel` model. All the priors for the CSM interaction models are same as in Subsection 6.1.2. In addition, we consider a uniform prior from $0.002 - 0.6$ for the nickel fraction in the ejecta ($f_{\rm Ni} = M_{\rm Ni}/M_{\rm ej}$).

The best-fitting parameters are listed in Table 5 and the best-fitting light curves are shown in Fig. 20. The 1σ errors listed represent only the statistical uncertainty associated with the fitting and therefore are not indicative of the model uncertainties.

From our estimated parameters, with the maximum allowed Ni mass of $\sim$0.04 $M_\odot$, we obtain a CSM mass of $\sim$0.22 $M_\odot$. We also obtain a small ejecta mass of 0.12 $M_\odot$. The constraint on the nickel (^{56}Ni) mass was overly prescriptive, resulting in an inferred value that was not constrained by the observational data. Consequently, the rest of the inferred parameters should be taken with a grain of salt. None the less, this modelling can serve as a comparison with studies using the same prescription for a combination of CSM and radioactivity powered SNe. The mass-loss rates estimated using the $R_{\rm CSM}$ of 0.10 AU, v_w of 1800 km s^{-1}, and density of $\rho_{\rm CSM}$ of 4.8 $\times$ 10^{-12} g cm^{-3}, is 3.9 $\times$ 10^{-4} $M_\odot$ yr^{-1}. In their sample study of five SNe Ibn, C. Pellegrino et al. (2022a) found that their light curves were well reproduced by ejecta masses between 0.7 and 3 $M_\odot$, CSM masses of $0.2 - 1$ $M_\odot$, and CSM radii between 20 and 65 AU. Our obtained values of CSM mass of 0.22 $M_\odot$ is consistent with the lower end of the CSM masses obtained by C. Pellegrino et al. (2022a), but our ejecta mass and radius are much lower than those found for the sample of SNe Ibn in C. Pellegrino et al. (2022a). The fits associated with both models infer that for the case of SN 2023xgo, ^{56}Ni plays a role in powering the late-time light curve. Since we do observe interaction signatures throughout the spectral evolution of SN 2023xgo, we introduce the CSM interaction in the light-curve modelling and find that both the CSM mass and the radius of the CSM are the lowest among the group of interacting SNe Ibn (C. Pellegrino et al. 2022a). As mentioned earlier, $M_{\rm Ni}$ was constrained to values ≤ 0.04 $M_\odot$ in order for the `csm_interaction` model to become non-neglible. The corner plots for both the CSM and the Ni + CSM models are shown in Figs A2 and A3, respectively.

Very low ejecta masses have also been seen for ultrastripped SNe (S. C. Wu & J. Fuller 2022; K. K. Das et al. 2024), but the rise time for SN 2023xgo is slower than for ultrastripped SNe (see Fig. 16). Recently, T. J. Moriya et al. (2025), through their theoretical modeling have found that in some cases ultrastripped SNe can result in Type Ibn SNe. The progenitors of the ultrastripped SNe can induce violent silicon burning phase just before the core-collapse that results in a dense CSM. They suggest that because the dense CSM is more massive than the SN ejecta, the ejecta is immediately decelerated and the light curve is powered mainly by the interaction due to which the ultrastripped SN is observed as a Type Ibn SN.

There are some caveats associated with the semi-analytical light-curve modelling and the parameters estimated. The simplifications

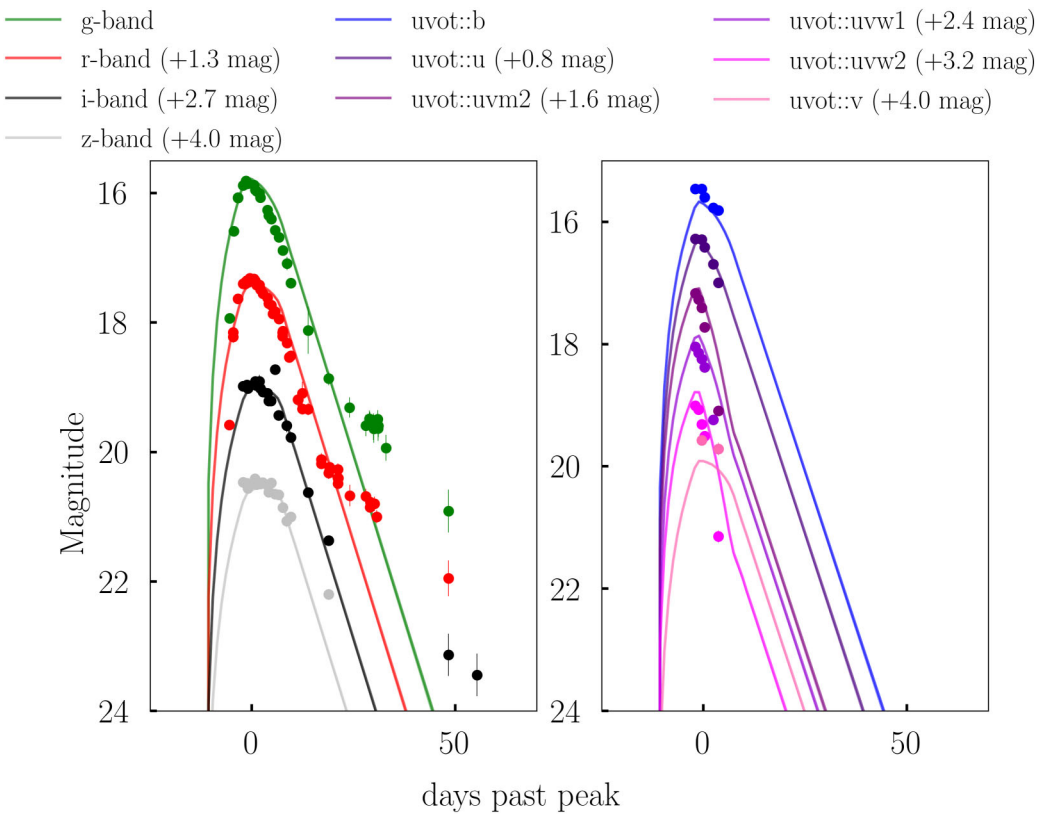

Figure 19. Multiband light-curve modelling using the CSM model by E. Chatzopoulos et al. (2012) as implemented in REDBACK. We see that SN 2023xgo is well reproduced using a CSM mass of 0.43 $M_\odot$ and a ejecta mass of 0.10 $M_\odot$. However, the model was not able to reproduce the late-time light-curve after 30 d past maximum.

Table 5. Table shows the best-fitting light-curve parameters from the CSM + Ni model. We note that the light curves are fairly reproduced by a high Ni mass and low ejecta and CSM masses than other SNe Ibn/Icn.

Parameters	Priors	Best-fitting values
$f_{\rm Ni}$	$\log\mathcal{U}$ [0.002, 0.6]	$0.324^{+0.001}_{-0.002}$
$M_{\rm ej}$ ($M_\odot$)	$\log\mathcal{U}$ [0.1, 15]	$0.1230^{+0.0002}_{-0.0002}$
$f_{\rm Ni}\cdot M_{\rm ej}$ ($M_\odot$)	$\log\mathcal{U}$ [0.001, 0.04]	$3.99^{+0.01}_{-0.03}\times10^{-2}$
$E_{\rm kin}$ (erg)	$\log\mathcal{U}$ [5×10^{49}, 10^{52}]	$5.005^{+0.068}_{-0.037}\times10^{49}$
$M_{\rm CSM}$ ($M_\odot$)	$\log\mathcal{U}$ [0.001, 15]	$22.147^{+0.003}_{-0.004}\times10^{-2}$
$T_{\rm floor}$ (K)	$\log\mathcal{U}$ [10^2, 10^4]	$7127.0^{+90.6}_{-98.1}$
t_0 (MJD)	$\mathcal{U}$ [$t_{\rm detection}-6$, $t_{\rm detection}$]	$60254.03^{+0.01}_{-0.01}$
η	$\mathcal{U}$ [0, 2]	$3.3^{+4.4}_{-2.4}\times10^{-3}$
ρ (g cm^{-3})	$\log\mathcal{U}$ [10^{-15}, 10^{-9}]	$4.8^{+0.1}_{-0.1}\times10^{-12}$
r_0 (AU)	$\log\mathcal{U}$ [10^{-1}, 10^2]	$0.104^{+0.006}_{-0.003}$

associated with the model and their possible implications are discussed further in Section 7.4. Also, the models by E. Chatzopoulos et al. (2012) assume a constant efficiency. Subsequently, we employ a non-equipartition light-curve model that incorporates the time-dependent evolution of radiative efficiency, accounting for the varying fraction of kinetic energy converted into observable radiation throughout the post-shock interaction and expansion phases.

6.2 Non-equipartition light-curve model

Even though the semi-analytical models did give us an estimate of CSM mass, radius and mass-loss rates, it did not take into account a time-varying efficiency conversion. We therefore also adopt a non-equipartition analytical light-curve model based on the formulation by K. Maeda & T. J. Moriya (2022) to reproduce our observed light curve.

The hydrodynamic evolution of the SN-CSM interaction, characterized by a forward shock (FS), contact discontinuity (CD), and a reverse shock (RS), is a classical problem with a well-developed solution. The evolution can be described by a self-similar solution as long as each of the ejecta and CSM structures is described by a single power law as a function of radius (which is the case when the reverse shock has not yet reached the inner, flat part of the ejecta). This hydrodynamic behaviour, or a simplified version thereof, is frequently used in light-curve calculations, where it is also often assumed that the post-shock regions quickly reach thermal equilibrium. K. Maeda & T. J. Moriya (2022) pointed out that the latter is not always the case; they modelled the light curves of a sample of SNe Ibn, including the physical processes in which high-energy photons created initially at the post-shock regions are eventually degraded to optical photons. They found that the flatter light-curve evolution is followed by a steeper evolution in the post-peak LCs, characterized by the transition of the shock properties from radiative to adiabatic. They consider the processes by which high-energy photons produced at the shocks are degraded to optical wavelengths, incorporating the effects of radiative cooling and the evolving optical depth of the CSM. In general, for a given CSM

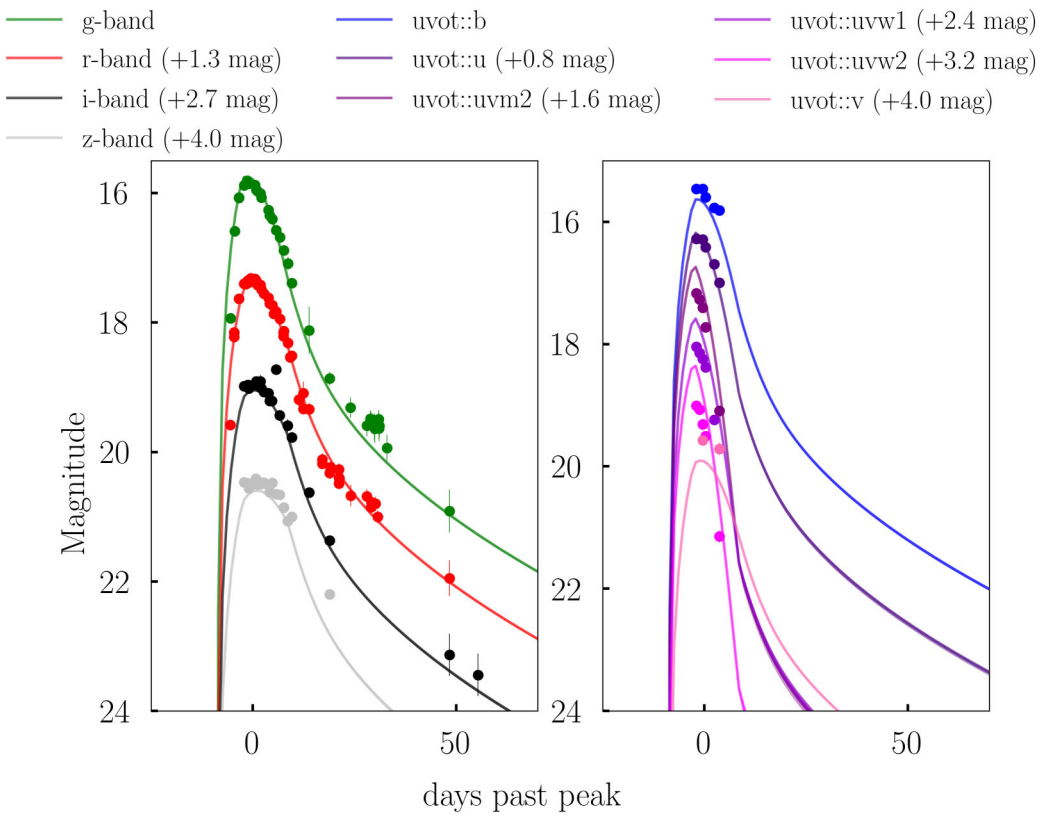

Figure 20. Multiband light-curve modelling using CSM + Ni by E. Chatzopoulos et al. (2012) using REDBACK. We see that SN 2023xgo is well reproduced using a ^{56}Ni mass of 0.04 $M_\odot$ (fixed), a CSM mass of 0.22 $M_\odot$, and a ejecta mass of 0.12 $M_\odot$.

density the optical luminosity in the model by K. Maeda & T. J. Moriya (2022) is smaller than in models like the one by E. Chatzopoulos et al. (2012, 2013) (i.e. the derived mass-loss rate is higher for any given LC data) since the conversion efficiency in most situations is found to be much lower than often assumed.

Given the limitations of the analytical CSM + Ni model, we are motivated to apply this more physically self-consistent LC model to SN 2023xgo. In the model, the SN ejecta are described by a broken power law in the density structure, where the inner density is constant and the outer part is given as $\rho_{\rm SN} \propto v^{-n}$ (e.g. R. A. Chevalier 1982; T. Moriya 2013). Here, $n = 7$ is fixed in the model, which is within the range expected for an explosion of a compact He star progenitor (C. D. Matzner & C. F. McKee 1999). The ejecta properties were described by the ejecta mass ($M_{\rm ej}$) and the kinetic energy ($E_{\rm k}$), which are varied as input parameters. For the CSM structure, a power-law distribution is assumed and the normalization constant of the distribution is set to 1 for a density of $\rho_{\rm CSM} = 10^{-14}$ g cm^{-3} and a radius of 5×10^{14} cm. The detailed set of equations relating the densities to the mass-loss rates of the progenitor is explained in K. Maeda & T. J. Moriya (2022, their section 3.1).

The models assume a He-rich composition for both SN ejecta and the CSM. Our best matched model parameters using the equations of the modelling section of K. Maeda & T. J. Moriya (2022) are

$M_{\rm ej} = 2.0\,M_\odot$ (fixed),
$E_{\rm k} = 1.7 \times 10^{51}$erg,
Ejecta slope (n) = 7 (fixed),
CSM slope (s) = 2.9,
$D' = 1.5$,

where D' is the normalization constant in the best matched density profile given by

$$\rho_{\rm CSM} = 10^{-14} D' \left(\frac{r}{5 \times 10^{14}\ {\rm cm}} \right)^{-s} \ {\rm g\ cm^{-3}}. \quad (4)$$

The model LC is shown in Fig. 21. We do not fit the early part of the light curve of SN 2023xgo, as diffusion is not taken into account while modelling the early part of the light curve of SN 2023xgo. The characteristic break at $\sim 10 - 20$ d since the explosion is explained by a transition in the shock properties (radiative to adiabatic) in this model, without introducing a change in the CSM density slope. The derived CSM density slope $s \sim 3$ is typical for SNe Ibn (as seen from the comparison of observational parameters by K. Maeda & T. J. Moriya 2022), indicating increasing mass-loss rate close to the explosion.

We note that the sample used in K. Maeda & T. J. Moriya (2022) is somewhat underluminous as compared to the larger SNe Ibn sample of G. Hosseinzadeh et al. (2017). SN 2023xgo falls in the low luminosity regime of the models by K. Maeda & T. J. Moriya (2022). Considering the best-fitting value of D' and using $v_w = 1800$ km s^{-1}, the mass-loss rate is estimated to be very high at $\sim$2.7 $M_\odot$ yr^{-1} (at 0.082 yr or 32.2 d before the explosion).

We note that the flatter light-curve tail could be fit by the ^{56}Co decay represented by the dashed line in Fig. 21, assuming $M_{\rm Ni} = 0.05\,M_\odot$ and taking into account the gamma-ray escape. Although this light-curve flattening could also be attributed to the CSM distribution being flattened in the outer regions, we mention the Co decay interpretation because of the spectral transition of SN 2023xgo from a SN Icn/Ibn with clear interaction signatures in the early phases (powered by the interaction) to a 'SN Ibn' without

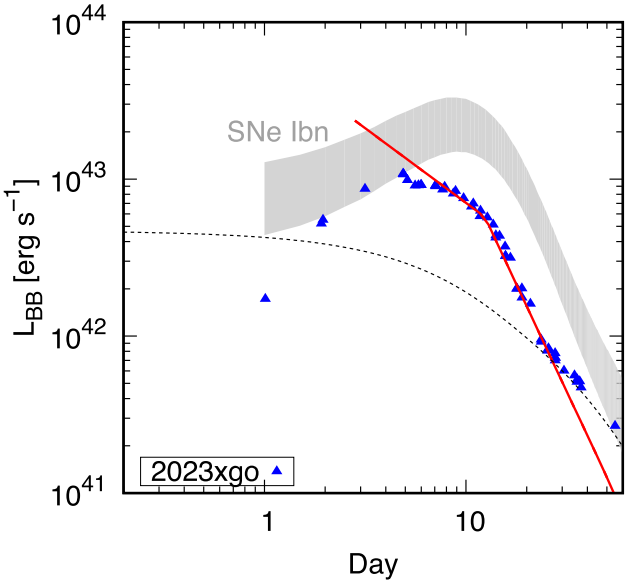

Figure 21. Fitting the light curve of SN 2023xgo with the models by K. Maeda & T. J. Moriya (2022). The grey shaded region shows the template light curve of SNe Ibn (G. Hosseinzadeh et al. 2017) while the red line shows the best-fitting model to the data of SN 2023xgo. The maximally allowed ^{56}Ni contribution is described by the black dashed line.

narrow lines in the late phase and even broad features (could be powered by radioactive decay) at even later times as discussed in the late phase spectral comparison in Subsection 3.3. The mass of ^{56}Ni in this scenario, 0.05 $M_\odot$, is similar to the values found for SNe IIP (M. Hamuy 2003), but smaller than those found for SNe Ibc (K. Maeda & T. J. Moriya 2022), and larger than the sample of SNe Ibn (C. Pellegrino et al. 2022a). We see that both our semi-analytical and non-equipartition light-curve model use $0.04 - 0.05$ $M_\odot$ of Ni to reproduce the late-time light curve. SN 2023xgo may thus be a link to investigate further a relation between interacting and non-interacting SESNe. However, using the semi-analytical model, the nickel mass (0.04 $M_\odot$) is set by the typical value from C. Pellegrino et al. (2022a). In the non-equipartition model by K. Maeda & T. J. Moriya (2022), the nickel mass is only estimated from the tail. This introduces a large uncertainty, so the interpretation of the nickel mass should be treated with caution.

7 DISCUSSION

We have presented the photometric and spectroscopic analysis of SN 2023xgo, and hereafter we discuss the main properties of the SN and summarize our results. We divide the SN evolution into three different phases: (a) pre-maximum time (−2.35 to 0 d), (b) maximum to late (before 23.48 d), and (c) late time (after 23.48 d), and briefly describe in each subsection the behaviour of the SN.

7.1 Pre-maximum times

SN 2023xgo is spectrally similar to a SN Icn, with prominent narrow C III lines at pre-maximum times. The early time spectral comparison of SN 2023xgo with other SNe Ibn and SNe Icn shows that the C III emission is stronger than for all SNe Ibn and also stronger than in the transitional SN 2023emq. While flash ionization may account for the observed features in SN 2023xgo, such an interpretation would require it to exhibit the strongest carbon signatures observed among all known SNe Ibn. The pseudo-EW measurements of the C III feature also highlights that this SN most likely belongs to the transitional SN Icn to SN Ibn category and is similar to a SN Icn at this early phase.

S. I. Blinnikov & E. I. Sorokina (2010) showed that the light curves of some Type I SNe can be modelled as a shock wave propagating in C-O-rich CSM material. SN 2023xgo probably has a C-O-He rich CSM. Assuming that part of the C III emission line enhancement arises from recombination or cascading transitions from C IV, we note that such processes typically involve ionization potentials exceeding 47 eV. This corresponds to a characteristic temperature above 50 000 K, indicating the presence of a high-energy radiation field or a hot ionizing source. This is the maximum temperature with the blackbody approximation. In reality, photoionization from non-thermal radiation fields (like UV/X-rays from shocks or interaction zones) can ionize carbon even at lower gas temperatures (C. Fransson & R. A. Chevalier 1989). Thus, in realistic SN environments, ionization can be driven by non-thermal radiation fields, allowing for significant C III populations even when the local gas temperature is substantially lower than 50 000 K. F. Martins & D. J. Hillier (2012) investigated the formation processes of C III λ5696 and C III λ4650 in the atmosphere of O stars using the non-LTE atmosphere code CMFGEN at two effective temperatures (30500 K and 42 000 K). The formation of the C III λ5696 line is governed by radiative interactions with nearby UV transitions (C III λ386, 574, and 884), which regulate the population levels of the lower and upper states involved. Line overlaps with metallic species such as Fe IV λ386, 574 and S V λ884 strongly influence emission strength through photon draining or enhancement. Variations in effective temperature, surface gravity, mass-loss rate, and metallicity further modulate the line profile, making C III λ5696 a very critical line profile derived from abundance diagnostic.

From Fig. 17 we see that the temperature for SN 2023xgo at early times is quite high, varying from 14 500 to 15 500 K, and then becomes constant at 9500 K a few days after maximum light, albeit with larger error bars associated with it. The temperature around maximum for SN 2023xgo is consistent with most SNe Ibn, but, still on the higher end (A. Gangopadhyay et al. 2020; T. Ben-Ami et al. 2023; S. J. Brennan et al. 2024; Y. Dong et al. 2024). The prolonged presence of carbon features in the spectra of SN 2023xgo, compared to typical SNe Ibn, may be attributed to a combination of elevated carbon abundance and sustained ionization driven by high temperatures in the early ejecta or CSM. The models by I. Boian & J. H. Groh (2019) show that the C III feature is better matched when the luminosity increases from 1.9 to 3.1 $\times$ 10^9 $L_\odot$. But, being a low luminosity member among the class (see Section 5), the temperature, elemental abundance and density must play the most important role for the case of SN 2023xgo in generating the C III λ5696 feature. The mass-loss rate of 10^{-3} $M_\odot$ yr^{-1} reproduces our observed spectral feature of C III at this phase.

Photometrically, SN 2023xgo behaves at this phase like a fast rising SN Ibn/Icn. The rise time of 5 d is consistent with all the SNe Ibn/Icn and shorter than that of Type II and Type Ib/c SNe. However, even if it photometrically resembles both SNe Ibn and SNe Icn at this phase, spectroscopically it is more similar to a SN Icn. If instead interpreted as a flash ionized SN Ibn, SN 2023xgo would be unique among its class with such a strong carbon emission.

7.2 From maximum to about 20 d past max

From maximum light, we see a transformation in the spectrum of SN 2023xgo. The C III λ5696 signature completely vanish and narrow He I lines develop throughout the evolution. The spectral

comparison at this epoch shows a strong similarity with SNe Ibn (G. Hosseinzadeh et al. 2017) and the spectra are also very similar to the transitional Type Ibn/Icn SN 2023emq (M. Pursiainen et al. 2023). This phase shows increasing velocities of the emission lines of He I λ5876, from 1800 km s^{-1} to about 10 000 km s^{-1}. This is also the phase when the P-Cygni He I signatures broaden and are taken over by emission with time.

At peak, SN 2023xgo is among the faintest events ($M_r = -17.65 \pm 0.04$ mag) within the SN Ibn/Icn population, exhibiting a decline rate of 0.14 mag d^{-1}, which is typical of this class. In Section 5 we show that SN 2023xgo is one of the lowest luminosity members of the SN Ibn/Icn family. As the luminosity declines, the temperature decreases accordingly, leading to recombination of carbon and the subsequent emergence of emission features of He I characteristic of typical SNe Ibn. At this phase, temperature also drops to 9500 K, leading to simultaneous emergence of emission signatures from He I, which require lower ionization energies. This spectroscopic transition, along with the coexistence of ionized and neutral features over time, may suggest a CSM with varying density and temperature structures.

7.3 Late-time emission

After 24 d, SN 2023xgo enters a phase in which both the ejecta and the CSM is optically thin. Spectral comparison with the models by L. Dessart et al. (2022) reproduce our late-phase spectrum with a low-mass He-star model of 3 $M_\odot$ assuming the CDS is at 2×10^{15} cm and we see spectral signatures of both ejecta and CSM at this phase. We also see a possible evidence of eruptive mass-loss activity from late-time light-curve and spectral modelling. Concurrently, the light curve exhibits a late-phase flattening, which might be explained by radioactive decay from ∼0.04 to 0.05 $M_\odot$ of synthesized ^{56}Ni. This estimated Ni mass is comparable to values typically inferred for core-collapse SNe II and SNe Ib/c, indicating a substantial contribution from radioactive heating. However, additional contributions from ongoing ejecta–CSM interaction cannot be ruled out, particularly given the asymmetry suggested by the spectral modelling. The spectral and photometric features at these phases collectively suggest the presence of a dense, extended CSM component indicative of an eruptive pre-SN mass-loss episode, further supported by the high mass-loss rates required by both light-curve and spectral models.

7.4 Caveats associated with the light-curve and spectral models

We have used a number of spectral and photometric models to try to draw conclusions about the nature of the transitioning SN Ibn/Icn 2023xgo. From the I. Boian & J. H. Groh (2019) spectral models (see Subsection 3.1.1) were able to reproduce the observed flash ionized lines of carbon, nitrogen, and helium. Increase in luminosity strengthened the C III λ5696 emission line. Since SN 2023xgo is one of the lowest luminosity members in the subclass (see Section 5), there must be other factors like density, temperature, and abundance which play an important role in the formation of the strong carbon signature. The model with a mass-loss rate of 10^{-3} $M_\odot$ yr^{-1} best matches our observed spectrum when the inner radius of the CSM is fixed at 8.6×10^{13} cm. However, the models by I. Boian & J. H. Groh (2019) are not radiatively post-processed and assume a fixed CSM inner radius at a fixed time. Thus, the estimates are valid only for these simplistic assumptions.

Late-time spectral comparison with models of L. Dessart et al. (2022) indicates that the model from a low mass He star of 3 $M_\odot$ and a spectral model luminosity of 2×10^{42} erg s^{-1} best matches our observed spectral feature of C III, while the observed luminosity is lower (6.0×10^{41} erg s^{-1}) at similar phases. However, this assumes that the CDS is located at 2×10^{15} cm. Also, the best matched model by L. Dessart et al. (2022) assume a CDS mass of ∼0.97 $M_\odot$ and an ejecta mass of 1.5 $M_\odot$. This corresponds to a mass-loss rate of approximately 0.16 M⊙ yr^{-1}, assuming $v_w = 1800$ km s^{-1}, consistent with an eruptive mass-loss scenario (N. Smith 2017).

We perform semi-analytical light-curve modelling using `redback` in Subsections 6.1.1, 6.1.2, and 6.1.3, assuming radioactivity, CSM interaction and both radioactivity + CSM driving the light-curve evolution of SN 2023xgo. The mass-loss rates (10^{-4}–10^{-3} $M_\odot$ yr^{-1}) and the radius of the CSM (∼ 10^{12}–10^{13} cm) that we get from semi-analytical models are similar to the values in the I. Boian & J. H. Groh (2019) models. If we consider an eruptive mass-loss case, then assuming a wind velocity of 1800 km s^{-1} and radius from Table 5, we would find that the shell would be ejected approximately few hours before the explosion. The semi-analytical models, however, assume spherical symmetry and homologous expansion, which may not fully represent the complexity of the CSM geometry. Viewing angle effects and 2D/3D structure could significantly alter the obtained parameters (A. Suzuki, T. J. Moriya & T. Takiwaki 2019; B. F. A. Baal et al. 2023).

In the semi-analytical light-curve modelling, the time-varying conversion of efficiency is not taken into account. So, we also perform late-time light-curve modelling following K. Maeda & T. J. Moriya (2022), which calculates a time varying efficiency throughout the light-curve evolution. For a given CSM density, the optical luminosity in the model by K. Maeda & T. J. Moriya (2022) is smaller than in models by E. Chatzopoulos et al. (2012, 2013). This gives us a higher mass-loss rate since the conversion efficiency at each time interval is much lower than often assumed in the semi-analytical approach. Using this model, we obtain a mass-loss rate of 2.7 $M_\odot$ yr^{-1} which suggests intense eruptive mass-loss occurring shortly before core collapse. While this value aligns with the upper limits of the eruptive scenarios modelled by L. Dessart et al. (2022), it still represents one of the most extreme cases in terms of pre-SN mass-loss rates. This model is not able to reproduce the early part of the light curve as diffusion was not taken into account (pre-maximum times).

E. Sorokina et al. (2016) performed `STELLA` models for the light curves of superluminous SNe I and found significant differences in the numerical model parameters as compared to E. Chatzopoulos et al. (2012) (see fig. 14 of E. Sorokina et al. 2016). They quote that this is probably due to very different diffusion time-scales and envelope masses in their light-curve modelling. We note that neither the CSM nor the SN ejecta can be approximated by a single zone velocity (T. J. Moriya et al. 2017). Thus, there are caveats associated with these models, but we do infer some constraints on the geometry and the physical parameters of SN 2023xgo by combining them which we describe in detail in Subsection 7.5.

7.5 Implications on geometry and possible progenitor

The early-time characteristics, when interpreted using the flash ionization models of I. Boian & J. H. Groh (2019) for the spectra and the semi-analytical framework of E. Chatzopoulos et al. (2012) for the light curve, indicate the presence of a compact CSM confined within a radius of ∼ 10^{12}–10^{13} cm. The inferred mass-loss rates in this phase are modest, on the order of 10^{-3}–10^{-4} $M_\odot$ yr^{-1}, consistent with a relatively quiescent, wind-driven phase prior to explosion. In contrast, modelling of the late-time light-curve following the approach of K. Maeda & T. J. Moriya (2022), along with spectral synthesis model comparisons by L. Dessart et al. (2022), reveals the

presence of an extended, dense CSM reaching out to $\sim 10^{15}$ cm, with significantly higher mass-loss rates ranging from 0.1 to 2.7 $M_\odot$ yr^{-1}. These findings may suggest a structured and possibly asymmetric CSM, composed of both compact, low-density material and a more extended, high-density component. However, such interpretations are model-dependent and could also arise from variations in the mass-loss history or radial density structure of the CSM, without necessarily invoking strong asymmetry. Multiple mass-loss episodes with differing energetics and geometries – potentially shaped by binary interaction, rotationally driven outflows, or eruptive events – could contribute to this complex CSM morphology.

The high mass-loss rates inferred from late-time modelling are consistent with eruptive phases in luminous blue variable stars transitioning to the WR phase (N. Smith 2017), which could indicate a single massive star as the progenitor of SN 2023xgo. However, if the CSM is asymmetric as indicated above with potential disc- or torus-like morphology, then it may also point toward a binary system. The modest helium-rich shell mass, likely originating from He-C and He-N layers, aligns with the 0.97 $M_\odot$ He-shell mass typically assumed in the models of L. Dessart et al. (2022). These constraints limit the pre-SN mass to $3-4$ $M_\odot$ and suggest a ZAMS mass not exceeding 18 $M_\odot$. Given that the 3 $M_\odot$ model best matches the nebular spectrum, a binary origin involving low-mass stars such as He stars, becomes more plausible, as stellar winds from red supergiants at these masses are insufficient to fully strip the hydrogen envelope (E. R. Beasor et al. 2020).

Furthermore, theoretical predictions suggest that standard WR explosions with decelerated inner shells (2000 km s^{-1}) should yield superluminous SNe (L. Dessart et al. 2016, 2022). However, as shown in Section 5, SN 2023xgo is among the least luminous events within the SN Ibn/Icn population. This again supports progenitor scenarios involving binary systems, such as nuclear flashes in low-mass helium stars (S. E. Woosley 2019; L. Dessart et al. 2022; Z. Y. Wang et al. 2024), or repeated mass-transfer episodes in compact binaries (N. Langer 2012; T. M. Tauris et al. 2013). Furthermore, the similarity in ejecta mass between SN 2023xgo and ultrastripped SNe reinforces the hypothesis of a low-mass helium star (ZAMS mass $\leq$10 $M_\odot$) in a close binary configuration, as proposed for SN 2023zaw (K. K. Das et al. 2024). The progenitor properties are further supported by the host Galaxy's stellar mass and star formation rate, which are similar to that of the general properties observed for the broader SN Ibn/Icn population.

8 SUMMARY

(i) SN 2023xgo is a unique member of the interacting SN Ibn/Icn class. It shows a prominent C III λ5696 spectral feature until maximum light, similar to what is seen for SNe Icn, but spectrally behaves like a typical SN Ibn with narrow helium lines post maximum light.

(ii) Comparison of the early spectrum (-2.35 d) with models by I. Boian & J. H. Groh (2019) indicates that even if the other flash features matches when $L = 1.5\times$ 10^9 $L_\odot$, the C III λ5696 feature only matches if L is increased to 3.1×10^9 $L_\odot$, with a mass-loss rate of 10^{-3} $M_\odot$ yr^{-1}.

(iii) Early spectral comparison (-2.35 d) and pseudo-equivalent width measurement of this C III λ5696 line indicates that the strength and evolution of this line behaves similarly to what is seen for other SNe Icn. If SN 2023xgo is classified as a SN Ibn with flash ionized signatures, the sustained detection of C III emission until maximum light suggests either a comparatively enhanced carbon abundance or temperatures capable of sustaining significant carbon ionization throughout the early evolution

(iv) The mid-spectral epoch (just after maximum light) marks the phase when SN 2023xgo behaves like a normal SN Ibn with narrow P-Cygni He I λ5876 and other helium lines with typical FWHM velocities starting around 1800 km s^{-1}. Spectral comparison at this phase with other SNe Ibn and SNe Icn also shows that it belongs to the 'P-Cygni' subclass according to G. Hosseinzadeh et al. (2017).

(v) After 10 d, ejecta signatures start appearing in the spectral evolution of SN 2023xgo. Late-time spectral comparison shows similarities with SN 2019wep, ASASSN-15ed, and some other SNe Ib.

(vi) Comparison of the 23.48 d spectrum with the models by L. Dessart et al. (2022) favours a 3 $M_\odot$ He-star model with the CDS located at 2.1×10^{15} cm.

(vii) The pseudo-equivalent widths of the He I lines in SN 2023xgo shows an increase up to 30 Å in 10 d, and velocities varying between 1800 and 10 000 km s^{-1} in 25 d. This value is higher than SN 2019wep and ASASSN-15ed and is similar to the velocity measurements for some SNe Ib at this phase.

(viii) The host Galaxy mass of $10^{9.31^{+0.13}_{-0.22}}$ $M_\odot$, metallicity of 0.7 ± 0.1 solar and the star-formation rate of 0.05 ± 0.02 $M_\odot$ yr^{-1} is similar to that of the sample of SNe Ibn/Icn.

(ix) Photometrically, SN 2023xgo behaves like a traditional SN Ibn/Icn with a rise time of 5.14 ± 2.30 d and decline rate ($0-30$ d) of 0.14 mag d^{-1}, similar to that of the values estimated from the larger sample of SNe Ibn/Icn (G. Hosseinzadeh et al. 2017; C. Pellegrino et al. 2022a, b).

(x) Comparisons between rise times, Δm_{15} and absolute magnitudes with a group of fast transients, SNe IIn, Ibn, Icn, and ultrastripped SNe indicate that the decline rates of SN 2023xgo are similar to that of those of SNe Ibn/Icn and are slower than the decline rates of fast transients and ultrastripped SNe.

(xi) The absolute magnitude of $M_r = -17.65 \pm 0.04$ places SN 2023xgo among the faintest members of the Type Ibn/Icn subclass, similar to SNe Ib.

(xii) Multiband modelling (semi-analytic) of SN 2023xgo indicates that CSM interaction fairly reproduces the early light curve, but radioactivity plays a role in reproducing the overall light curve of SN 2023xgo, specially at late times. The light curve seems to be driven by a CSM mass of $\sim$0.22 $M_\odot$, and a small ejecta mass of 0.12 $M_\odot$, assuming its radioactivity driven with Ni mass of 0.04 $M_\odot$. A shell-like CSM with a radius of 10^{12} cm is favoured by our observed data.

(xiii) Late-time bolometric light-curve modelling fairly reproduces the light curve with a density exponent of 2.9, CSM extent at 10^{15} cm and mass-loss rates of 2.7 $M_\odot$ yr^{-1}. A Ni mass of 0.05 $M_\odot$ reproduces the late-time light-curve if we assume radioactivity to be powering the light curve.

(xiv) Overall,the inferred mass-loss rates suggest two distinct CSM components: a compact, low-density region ($\sim 10^{-3}$ $M_\odot$ yr^{-1} at 10^{12}–10^{13} cm) and an extended, dense region ($0.1-2.7$ $M_\odot$ yr^{-1} at $\sim 10^{15}$ cm). This structure may result from asymmetric geometry or reflect temporal and radial variations in mass-loss history, though such interpretations remain model-dependent.

(xv) The combination of a likely asymmetric CSM structure and spectral characteristics is similar to that of a binary progenitor system for SN 2023xgo, potentially involving a $\sim$3 $M_\odot$ helium star. None the less, the observed indications of eruptive mass-loss do not exclude a single-star origin, especially in the context of advanced evolutionary phases that may produce non-steady outflows.

ACKNOWLEDGEMENTS

This work has been enabled by support from the research project grant 'Understanding the Dynamic Universe' funded by the Knut

and Alice Wallenberg under Dnr KAW 2018.0067. Based on observations obtained with the Samuel Oschin Telescope 48-inch and the 60-inch Telescope at the Palomar Observatory as part of the Zwicky Transient Facility project. ZTF is supported by the National Science Foundation under Grant No. AST-2034437 and a collaboration including Caltech, IPAC, the Oskar Klein Center at Stockholm University, the University of Maryland, University of California, Berkeley, the University of Wisconsin at Milwaukee, University of Warwick, Ruhr University Bochum, Cornell University, Northwestern University and Drexel University. Operations are conducted by COO, IPAC, and UW. SED Machine is based upon work supported by the National Science Foundation under Grant No. 1106171. The ZTF forced-photometry service was funded under the Heising-Simons Foundation grant #12540303 (PI: Graham). The Gordon and Betty Moore Foundation, through both the Data-Driven Investigator Program and a dedicated grant, provided critical funding for SkyPortal. We thank Takashi J. Moriya and Masaomi Tanaka for insightful discussion about the paper. KM acknowledges support from the Japan Society for the Promotion of Science (JSPS) KAKENHI grant JP24KK0070 and JP24H01810. RD acknowledges funds by ANID grant FONDECYT Postdoctorado N°3220449. MS acknowledges financial support provided under the National Post Doctoral Fellowship (N-PDF; File Number: PDF/2023/002244) by the Science and Engineering Research Board (SERB), Anusandhan National Research Foundation (ANRF), Government of India. NS and AS acknowledges support from the Knut and Alice Wallenberg Foundation through the 'Gravity Meets Light' project and by the research environment grant 'Gravitational Radiation and Electromagnetic Astrophysical Transients' (GREAT) funded by the Swedish Research Council (VR) under Dnr 2016–06012.

The spectrum taken by the Seimei telescope was obtained under the KASTOR (Kanata And Seimei Transient Observation Regime) project, specifically under the following program for the Seimei Telescope at the Okayama observatory (23B-K-0013 and 23B-N-CT11). The Seimei telescope at the Okayama Observatory is jointly operated by Kyoto University and the National Astronomical Observatory of Japan (NAOJ), with assistance provided by the Optical and Infrared Synergetic Telescopes for Education and Research (OISTER) program.

This work acknowledges the support of Prof. G. C. Anupama (Indian Institute of Astrophysics, Bengaluru) for facilitating the acquisition of observational data using the GROWTH-India Telescope.

The GROWTH-India telescope (GIT) is a 70 cm telescope with a 0.7° field of view set up by the Indian Institute of Astrophysics (IIA) and the Indian Institute of Technology Bombay (IITB) with funding from the Indo-US Science and Technology Forum and the Science and Engineering Research Board, Department of Science and Technology, Government of India. It is located at the Indian Astronomical Observatory (IAO, Hanle).

DATA AVAILABILITY

The data presented in this paper will be provided upon request. All the spectra will be made publicly available in WiseRep and Zenodo.

REFERENCES

Ambikasaran S., Foreman-Mackey D., Greengard L., Hogg D. W., O'Neil M., 2015, IEEE Trans. Pattern Anal. Mach. Intell., 38, 252
Arnett W. D., 1982, ApJ, 253, 785
Ashton G., et al., 2019, ApJS, 241, 27
Astropy Collaboration, 2022, ApJ, 935, 167
Balcon C., 2023, Transient Name Server Classification Report, 2023-2931, 1
Barden S. C., 1994, in Pyper D. M., Angione R. J., eds, ASP Conf. Ser. Vol. 55, Optical Astronomy from the Earth and Moon. Astron. Soc. Pac., San Francisco, p. 130
Beasor E. R., Davies B., Smith N., van Loon J. T., Gehrz R. D., Figer D. F., 2020, MNRAS, 492, 5994
Becker A., 2015, record ascl:1504.004
Bellm E. C. et al., 2019, PASP, 131, 068003
Ben-Ami T. et al., 2023, ApJ, 946, 30
Bertin E., 2013, record ascl:1301.001
Blagorodnova N. et al., 2018, PASP, 130, 035003
Blinnikov S. I., Sorokina E. I., 2010, preprint (arXiv:1009.4353)
Boian I., Groh J. H., 2019, A&A, 621, A109
Bradley L. et al., 2024, astropy/photutils: 1.13.0, Zenodo. Available at: https://doi.org/10.5281/zenodo.12585239
Brennan S. J. et al., 2024, A&A, 690, A259
Bruch R. J. et al., 2021, ApJ, 912, 46
Bruch R. J. et al., 2023, ApJ, 952, 119
Burrows D. N. et al., 2005, Space Sci. Rev., 120, 165
Byler N., Dalcanton J. J., Conroy C., Johnson B. D., 2017, ApJ, 840, 44
Calzetti D., Armus L., Bohlin R. C., Kinney A. L., Koornneef J., Storchi-Bergmann T., 2000, ApJ, 533, 682
Cao Y. et al., 2013, ApJ, 775, L7
Cardelli J. A., Clayton G. C., Mathis J. S., 1989, ApJ, 345, 245
Carrick J., Turnbull S. J., Lavaux G., Hudson M. J., 2015, MNRAS, 450, 317
Chabrier G., 2003, PASP, 115, 763
Chambers K. C., Pan-STARRS Team, 2016, American Astronomical Society, AAS Meeting #227, id.324.07
Chatzopoulos E., Wheeler J. C., Vinko J., 2012, ApJ, 746, 121
Chatzopoulos E., Wheeler J. C., Vinko J., Horvath Z. L., Nagy A., 2013, ApJ, 773, 76
Chevalier R. A., 1982, ApJ, 258, 790
Colgate S. A., McKee C., 1969, ApJ, 157, 623
Conroy C., Gunn J. E., White M., 2009, ApJ, 699, 486
Coughlin M. W. et al., 2023, ApJS, 267, 31
Craig M. et al., 2017, astropy/ccdproc: v1.3.0.post1, Zenodo. Available at:https://doi.org/10.5281/zenodo.1069648
Curti M., Cresci G., Mannucci F., Marconi A., Maiolino R., Esposito S., 2017, MNRAS, 465, 1384
Das K. K. et al., 2024, ApJ, 969, L11
Dekany R. et al., 2020, PASP, 132, 038001
Dessart L., 2024, Supernova Remnants III: An Odyssey in Space after Stellar Death. Chania, Crete, Greece, p. 37
Dessart L., Hillier D. J., Audit E., Livne E., Waldman R., 2016, MNRAS, 458, 2094
Dessart L., Hillier D. J., Kuncarayakti H., 2022, A&A, 658, A130
Dong Y. et al., 2024, ApJ, 977, 254
Drout M. R. et al., 2014, ApJ, 794, 23
Ertl T., Woosley S. E., Sukhbold T., Janka H. T., 2020, ApJ, 890, 51
Evans P. A. et al., 2007, A&A, 469, 379
Evans P. A. et al., 2009, MNRAS, 397, 1177
Falk S. W., Lattimer J. M., Margolis S. H., 1977, Nature, 270, 700
Fassia A. et al., 2001, MNRAS, 325, 907
Flewelling H. A. et al., 2020, ApJS, 251, 7
Foley R. J., Smith N., Ganeshalingam M., Li W., Chornock R., Filippenko A. V., 2007, ApJ, 657, L105
Foreman-Mackey D., Sick J., Johnson B., 2014, Python-Fsps: Python Bindings To Fsps (V0.1.1), Zenodo
Fransson C., Chevalier R. A., 1989, ApJ, 343, 323
Fraser M., 2020, R. Soc. Open Sci., 7, 200467
Fremling C. et al., 2014, A&A, 565, A114
Fremling C. et al., 2016, A&A, 593, A68
Fremling C., 2023, Transient Name Server Discovery Report, 2023-2892, 1
Gal-Yam A. et al., 2014, Nature, 509, 471
Gal-Yam A. et al., 2022, Nature, 601, 201
Gangopadhyay A. et al., 2020, ApJ, 889, 170
Gangopadhyay A. et al., 2022, ApJ, 930, 127

Gangopadhyay A. et al., 2025, MNRAS, 537, 2898
Gangopadhyay A., 2024, preprint (arXiv:2411.04107)
Gehrels N. et al., 2004, ApJ, 611, 1005
Graham M. J. et al., 2019, PASP, 131, 078001
Hamuy M., 2003, ApJ, 582, 905
HI4PI Collaboration 2016, A&A, 594, A116
Ho A. Y. Q. et al., 2023, ApJ, 949, 120
Hosseinzadeh G. et al., 2017, ApJ, 836, 158
Hunter J. D., 2007, Comput. Sci. Eng., 9, 90
Irani I. et al., 2024, ApJ, 970, 96
Johnson B. D., Leja J., Conroy C., Speagle J. S., 2021, ApJS, 254, 22
Karamehmetoglu E. et al., 2017, A&A, 602, A93
Karamehmetoglu E. et al., 2021, A&A, 649, A163
Kawabata K. S. et al., 2008, in McLean I. S., Casali M. M., eds, Proc. SPIE Conf. Ser. Vol. 7014, Ground-based and Airborne Instrumentation for Astronomy II. SPIE, Bellingham, p. 70144L
Kennicutt R. C. J., 1998, ARA&A, 36, 189
Khazov D. et al., 2016, ApJ, 818, 3
Kilpatrick C. D., Foley R. J., 2018, MNRAS, 481, 2536
Kim Y. L. et al., 2022, PASP, 134, 024505
Kool E. C. et al., 2021, A&A, 652, A136
Kumar H. et al., 2022, AJ, 164, 90
Lang D., 2014, AJ, 147, 108
Langer N., 2012, ARA&A, 50, 107
Lusk J. A., Baron E., 2017, PASP, 129, 044202
Madau P., Dickinson M., 2014, ARA&A, 52, 415
Maeda K., Moriya T. J., 2022, ApJ, 927, 25
Mainzer A. et al., 2014, ApJ, 792, 30
Mandigo-Stoba M. S., Fremling C., Kasliwal M. M., 2021, J. Open Source Softw., 7, 3612
Mandigo-Stoba M. S., Fremling C., Kasliwal M. M., 2022a, DBSP_DRP: A Python package for automated spectroscopic data reduction of DBSP data, Zenodo. Available at: https://doi.org/10.5281/zenodo.6241526
Mandigo-Stoba M. S., Fremling C., Kasliwal M. M., 2022b, J. Open Source Softw., 7, 3612
Martins F., Hillier D. J., 2012, A&A, 545, A95
Masci F. J. et al., 2019, PASP, 131, 018003
Matsubayashi K. et al., 2019, PASJ, 71, 102
Matzner C. D., McKee C. F., 1999, ApJ, 510, 379
McCully C., Tewes M., 2019, record ascl:1907.032
Meisner A. M., Lang D., Schlegel D. J., 2017, AJ, 153, 38
Moriya T. J., Mueller B., Blinnikov S. I., Ushakova M., Sorokina E. I., Tauris T. M., Heger A., 2025, Publ. Astron. Soc. Japan, 77, 1385
Moriya T. J., Yoon S.-C., Gräfener G., Blinnikov S. I., 2017, MNRAS, 469, L108
Moriya T., 2013, PhD thesis, University of Tokyo, Department of Astronomy
Nagao T. et al., 2023, A&A, 673, A27
Nicholl M., 2018, Res. Notes Am. Astron. Soc., 2, 230
Oke J. B. et al., 1995, PASP, 107, 375
Oke J. B., 1990, AJ, 99, 1621
Oke J. B., Gunn J. E., 1982, PASP, 94, 586
Osterbrock D. E., Ferland G. J., 2006, Astrophysics of Gaseous Nebulae and Active Galactic Nuclei, 2nd. ed. University Science Books, Sausalito, CA
Pastorello A. et al., 2007, Nature, 447, 829
Pastorello A. et al., 2015a, MNRAS, 449, 1921
Pastorello A. et al., 2015b, MNRAS, 449, 1941
Pastorello A. et al., 2015c, MNRAS, 453, 3649
Pellegrino C. et al., 2022a, ApJ, 926, 125
Pellegrino C. et al., 2022b, ApJ, 938, 73
Perley D. A. et al., 2019, MNRAS, 484, 1031
Perley D. A. et al., 2020, ApJ, 904, 35
Perley D. A. et al., 2022, ApJ, 927, 180
Piascik A. S., Steele I. A., Bates S. D., Mottram C. J., Smith R. J., Barnsley R. M., Bolton B., 2014, in Ramsay S. K., McLean I. S., Takami H., eds, Proc. SPIE Conf. Ser. Vol. 9147, Ground-based and Airborne Instrumentation for Astronomy V. SPIE, Bellingham, p. 91478H
Poznanski D., Prochaska J. X., Bloom J. S., 2012, MNRAS, 426, 1465
Prabhu T. P., Anupama G. C., 2010, in Ojha D.K., ed., ASI Conf. Ser. Vol. 1, Interstellar Matter and Star Formation: A Multi-wavelength Perspective. Indian Astronomical Observatory, Hanle
Prochaska J. X. et al., 2019, pypeit/PypeIt: Releasing for DOI, Zenodo
Prochaska J. X. et al., 2020, J. Open Source Softw., 5, 2308
Prochaska J. X. et al., 2021, pypeit/PypeIt: Version 1.6.0, Zenodo. Available at: https://doi.org/10.5281/zenodo.5548381
Pursiainen M. et al., 2023, ApJ, 959, L10
Qin Y.-J., Zabludoff A., 2024, MNRAS, 533, 3517
Riess A. G. et al., 2011, ApJ, 730, 119
Rigault M. et al., 2019, A&A, 627, A115
Roberson M., Fremling C., Kasliwal M., 2022, J. Open Source Softw., 7, 3612
Roming P. W. A. et al., 2005, Space Sci. Rev., 120, 95
Sarin N. et al., 2024, MNRAS, 531, 1203
Schlafly E. F., Finkbeiner D. P., 2011, ApJ, 737, 103
Schulze S. et al., 2021, ApJS, 255, 29
Schulze S. et al., 2025, Nature, 644, 634
Shivvers I. et al., 2016, MNRAS, 461, 3057
Skrutskie M. F. et al., 2006, AJ, 131, 1163
Smith N., 2017, in Alsabti A. W., Murdin P., eds, Handbook of Supernovae. Springer, Cham, p. 403
Smith N., Li W., Silverman J. M., Ganeshalingam M., Filippenko A. V., 2011, MNRAS, 415, 773
Sollerman J., Chu M., Dahiwale A., Fremling C., 2023, Transient Name Server Classification Report, 2023-3181, 1
Sorokina E., Blinnikov S., Nomoto K., Quimby R., Tolstov A., 2016, ApJ, 829, 17
Speagle J. S., 2020, MNRAS, 493, 3132
Steele I. A. et al., 2004, in Oschmann J. M., Jr, ed., Proc. SPIE Conf. Ser. Vol. 5489, Ground-based Telescopes. SPIE, Bellingham, p. 679
Sun N.-C., Maund J. R., Hirai R., Crowther P. A., Podsiadlowski P., 2019, MNRAS, 491, 6000
Suzuki A., Moriya T. J., Takiwaki T., 2019, ApJ, 887, 249
Tauris T. M., Sanyal D., Yoon S. C., Langer N., 2013, A&A, 558, A39
Teja R. S. et al., 2023, ApJ, 954, L12
Tody D., 1986, in Crawford D. L., ed., Proc. SPIE Conf. Ser. Vol. 627, Instrumentation in Astronomy VI. SPIE, Bellingham, p. 733
Valenti S. et al., 2008, MNRAS, 383, 1485
van Baal B. F. A., Jerkstrand A., Wongwathanarat A., Janka H.-T., 2023, MNRAS, 523, 954
van der Walt S. J., Crellin-Quick A., Bloom J. S., 2019, J. Open Source Softw., 4, 1247
van der Walt S., Colbert S. C., Varoquaux G., 2011, Comput. Sci. Eng., 13, 22
van Dokkum P. G., 2001, PASP, 113, 1420
Van Dyk S. D. et al., 2018, ApJ, 860, 90
Virtanen P. et al., 2020, scipy/scipy: SciPy 1.6.0, Zenodo
Wang Z. Y. et al., 2024, A&A, 691, A156
Woosley S. E., 2019, ApJ, 878, 49
Woosley S. E., Weaver T. A., 1995, ApJS, 101, 181
Wright A. H. et al., 2016, MNRAS, 460, 765
Wright E. L. et al., 2010, AJ, 140, 1868
Wu S. C., Fuller J., 2022, ApJ, 940, L27
Yaron O., Gal-Yam A., 2012, PASP, 124, 668

SUPPORTING INFORMATION

Supplementary data are available at *MNRAS* online.

suppl_data

Please note: Oxford University Press is not responsible for the content or functionality of any supporting materials supplied by the authors. Any queries (other than missing material) should be directed to the corresponding author for the article.

APPENDIX: LIGHT-CURVE MODELLING RESULTS

A1. CSM + Ni model

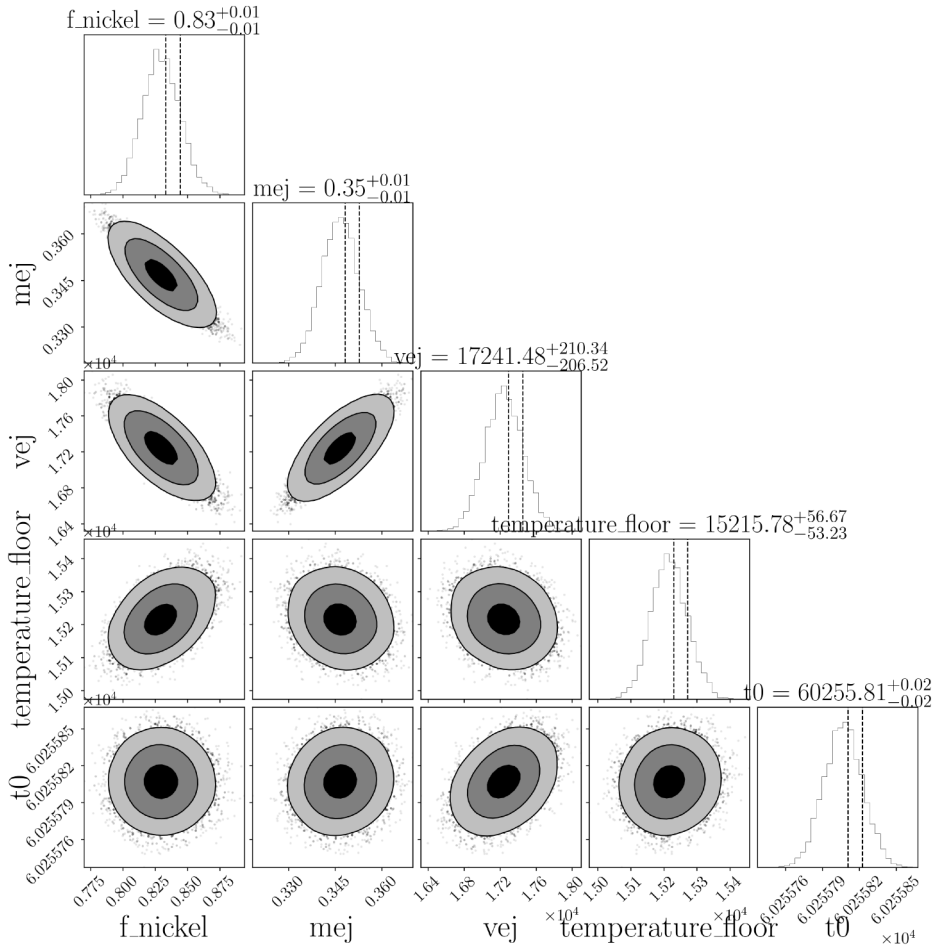

Figure A1. The corner plot showing the posterior of the parameters of SN 2023xgo in the radioactively powered model (W. D. Arnett 1982).

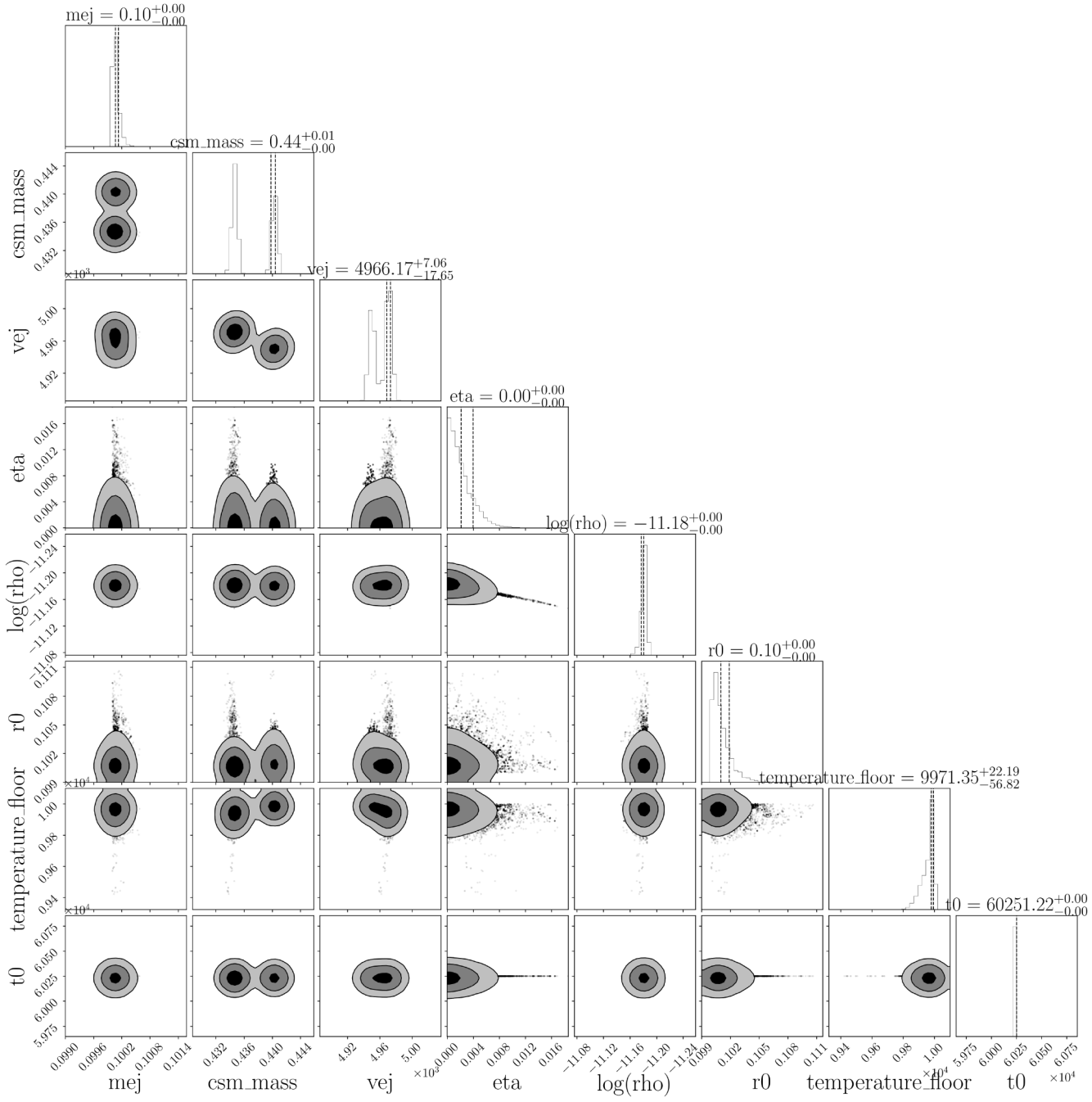

Figure A2. The corner plot showing the posterior of the parameters of SN 2023xgo in the CSM interaction model (E. Chatzopoulos et al. 2012, 2013).

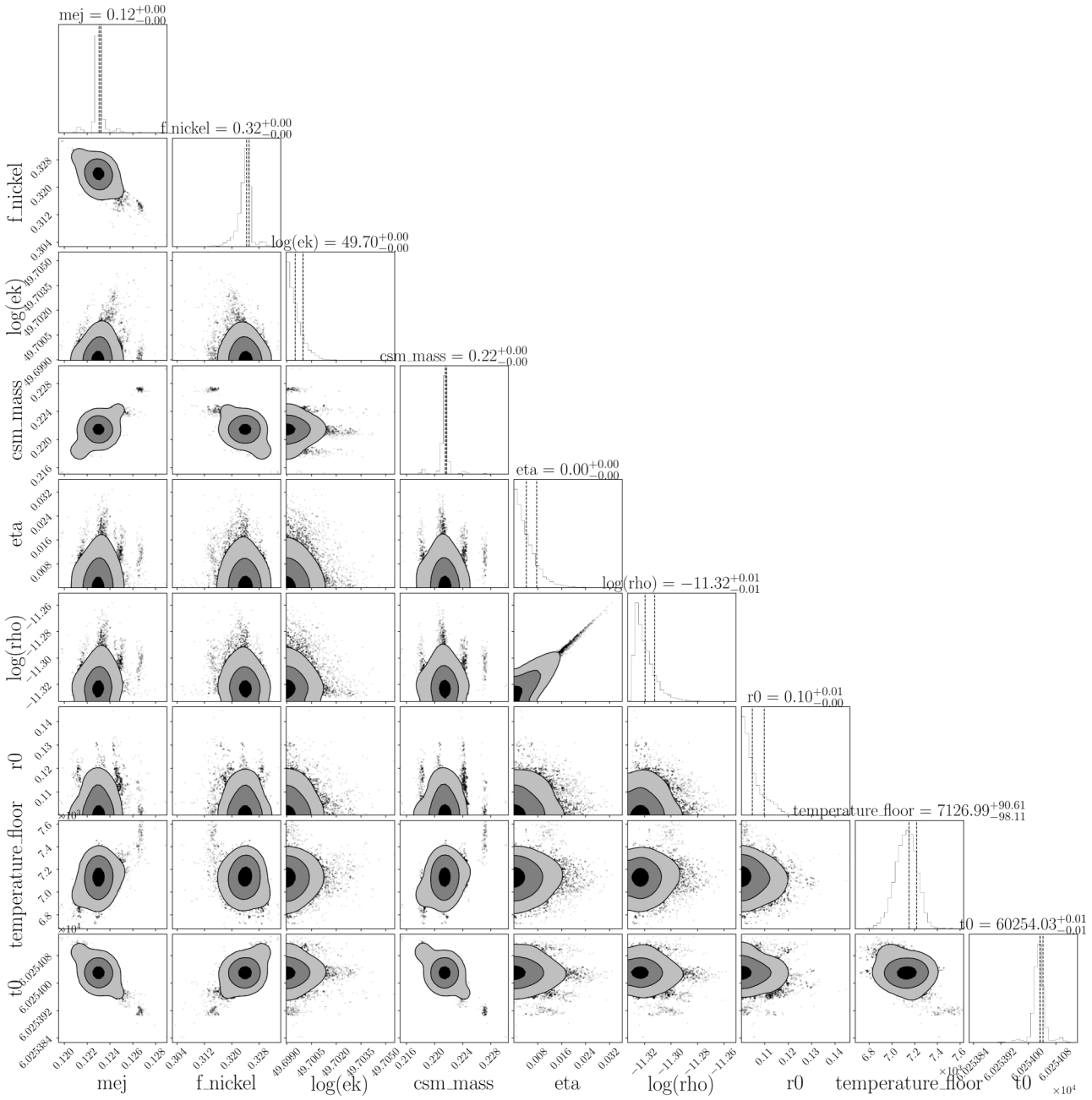

Figure A3. The corner plot showing the posterior of the parameters of SN 2023xgo in the Ni + CSM model (W. D. Arnett 1982; E. Chatzopoulos et al. 2012).

Table A1. A small section of the photometric observations of SN 2023xgo. The full table is added in machine readable format in supplementary material.

MJD (d)	Mag (mag)	Filter	Instrument/Telescope
60257.28	18.69 ± 0.07	r	ZTF/P48
60257.37	18.52 ± 0.03	g	ZTF/P48
60258.20	17.34 ± 0.09	r	SEDM/P60
60258.24	17.26 ± 0.03	r	SEDM/P60
60258.36	17.18 ± 0.01	g	ZTF/P48
60259.39	16.65 ± 0.01	g	ZTF/P48
60259.43	16.66 ± 0.01	g	ZTF/P48
60259.45	16.74 ± 0.01	r	ZTF/P48
60260.71	16.47 ± 0.04	g	GIT
60260.71	16.52 ± 0.01	r	GIT
60260.71	16.60 ± 0.03	i	GIT
60260.72	16.69 ± 0.06	z	GIT
60260.85	16.69 ± 0.03	uvot:uvw1	UVOT/Swift
60260.85	16.26 ± 0.04	uvot:u	UVOT/Swift
60260.85	16.11 ± 0.05	uvot:b	UVOT/Swift
60260.85	17.11 ± 0.03	uvot:uvw2	UVOT/Swift
60260.86	16.68 ± 0.09	uvot:v	UVOT/Swift
60260.86	17.05 ± 0.03	uvot:uvm2	UVOT/Swift
60261.19	16.52 ± 0.02	r	SEDM/P60
60261.22	16.49 ± 0.01	r	SEDM/P60
60261.43	16.39 ± 0.01	g	ZTF/P48
60261.45	16.49 ± 0.02	r	ZTF/P48
60261.63	16.71 ± 0.07	z	GIT
60261.64	16.58 ± 0.03	i	GIT
60261.64	16.47 ± 0.02	r	GIT
60261.64	16.44 ± 0.03	g	GIT

Table A2. Log of spectroscopic observations of SN 2023xgo. The phase (rest frame) is measured with respect to *r*-band maximum ($MJD_{rmax} = 60262.86$).

Date	Phase (d)	Instrument	Telescope	Range (Å)
20231112	−2.35	KOOLS-IFU	3.8 m Seime	4000–8000
20231113	−1.66	SEDM	Palomar 60	3650–10000
20231113	−0.82	SPRAT	Liverpool Telescope	4020–8100
20231114	−0.54	HFOSC	HCT	3800–8350
20231114	−0.07	SEDM	Palomar 60	3650–10000
20231115	0.53	SEDM	Palomar 60	3650–10000
20231115	0.53	DBSP	Palomar 200	3000–11000
20231117	2.64	KOOLS-IFU	3.8m Seimei	4000–8000
20231117	3.07	HFOSC	HCT	3800–8350
20231119	4.75	HFOSC	HCT	3800–8350
20231120	5.34	LRIS	KECK	3500–11000
20231120	5.39	SEDM	Palomar 60	3650–10000
20231122	7.63	SEDM	Palomar 60	3650–10000
20231123	8.64	KOOLS-IFU	3.8 m Seimei	4000–8000
20231124	9.30	SEDM	Palomar 60	3650–10000
20231125	10.97	HFOSC	HCT	3800–8350
20231202	17.31	SEDM	Palomar 60	3650–10000
20231203	18.42	DBSP	Palomar 200	3000–11000
20231206	21.48	SEDM	Palomar 60	3650–10000
20231207	23.48	LRIS	KECK	3500–11000

[1]*Oskar Klein Centre, Department of Astronomy, Stockholm University, AlbaNova, SE-106 91 Stockholm, Sweden*
[2]*Department of Astronomy, Kyoto University, Kitashirakawa-Oiwake-cho, Sakyo-ku, Kyoto 606-8502, Japan*
[3]*Aryabhatta Research Institute of Observational Sciences, Manora Peak 263001, India*
[4]*Department of Applied Physics, Mahatma Jyotiba Phule Rohilkhand University, Bareilly 243006, India*
[5]*Center for Interdisciplinary Exploration and Research in Astrophysics (CIERA), Northwestern University, 1800 Sherman Ave, Evanston, IL 60201, USA*
[6]*Oskar Klein Centre, Department of Physics, Stockholm University, AlbaNova, Stockholm SE-106 91, Sweden*
[7]*Indian Institute of Astrophysics, Koramangala 2nd Block, Bangalore 560034, India*
[8]*Astrophysics Research Institute, Liverpool John Moores University, IC2, Liverpool L3 5RF, UK*
[9]*Hiroshima Astrophysical Science Centre, Hiroshima University, 1-3-1 Kagamiyama, Higashi-Hiroshima, Hiroshima 739-8526, Japan*
[10]*Instituto de Astrofísica, Universidad Andres Bello, Fernandez Concha 700, Las Condes, Santiago RM 7591538, Chile*
[11]*Millennium Institute of Astrophysics, Nuncio Monsenor Sótero Sanz 100, Providencia, Santiago 8320000, Chile*
[12]*Cahill Center for Astrophysics, California Institute of Technology, MC 249-17, 1200 E California Boulevard, Pasadena, CA 91125, USA*
[13]*Caltech Optical Observatories, California Institute of Technology, Pasadena, CA 91125, USA*
[14]*Division of Physics, Mathematics, and Astronomy, California Institute of Technology, Pasadena, CA 91125, USA*
[15]*Department of Astronomy, Cornell University, Cornell, NY 14853 USA*
[16]*IPAC, California Institute of Technology, 1200 E. California Blvd, Pasadena, CA 91125, USA*
[17]*Department of Physics, Drexel University, Philadelphia, PA 19104, USA*

This paper has been typeset from a TEX/LATEX file prepared by the author.